

Analyzing the Uncertainty of Biomass Estimates From L-Band Radar Backscatter Over the Harvard and Howland Forests

Razi Ahmed, *Member, IEEE*, Paul Siqueira, *Member, IEEE*, and Scott Hensley, *Senior Member, IEEE*

Abstract—A better understanding of ecosystem processes requires accurate estimates of forest biomass and structure on global scales. Recently, there have been demonstrations of the ability of remote sensing instruments, such as radar and lidar, for the estimation of forest parameters from spaceborne platforms in a consistent manner. These advances can be exploited for global forest biomass accounting and structure characterization, leading to a better understanding of the global carbon cycle. The popular techniques for the estimation of forest parameters from radar instruments, in particular, use backscatter intensity, interferometry, and polarimetric interferometry. This paper analyzes the uncertainty in biomass estimates derived from single-season L-band cross-polarized (HV) radar backscatter over temperate forests of the Northeastern United States. An empirical approach is adopted, relying on ground-truth data collected during field campaigns over the Harvard and Howland Forests in 2009. The accuracy of field biomass estimates, including the impact of the diameter–biomass allometry, is characterized for the field sites. A single-season radar data set from the National Aeronautics and Space Administration Jet Propulsion Laboratory’s L-band Uninhabited Aerial Vehicle Synthetic Aperture Radar instrument is analyzed to assess the accuracy of the backscatter–biomass relationships with a theoretical radar error model.

Index Terms—Biomass, errors, Harvard Forest, Howland Forest, radar backscatter.

I. INTRODUCTION

IN RECENT years, there has been an ongoing effort in the remote sensing community to relate forest structural characteristics such as height, density, and biomass to remote sensing observations derived from optical, microwave, and other deployable sensors. To date, this effort has yielded successful results on small scales, as well as increasingly more accurate results over larger scales. However, there still remains a need for further development, particularly in terms of determining these characteristics at hectare resolutions and to accuracies on the order of tens of percent.

To address these needs, the National Research Council has released a recommendation [1] for the National Aeronautics and Space Administration (NASA) to pursue a spaceborne sen-

sor that is capable of achieving these accuracies on continental and global scales. An essential component of the proposed deformation, ecosystem structure and dynamics of ice (DESDynI) mission [2] is to use polarimetric radar measurements for estimating forest biomass at hectare-scale resolutions spanning the entire globe. For the last few years, there has been a concerted effort to demonstrate the feasibility of a DESDynI-like observation strategy and to assess the accuracy of various potential estimation methods in anticipation of such a mission.

In this paper, we describe one such effort which utilizes the Harvard and Howland Forests as the target sites for analysis and incorporates observations from the NASA/Jet Propulsion Laboratory (JPL) Uninhabited Aerial Vehicle Synthetic Aperture Radar (UAVSAR) instrument. We begin by first highlighting results from an intensive ground validation effort that was carried out in the region in the summer of 2009 [3], the same time that the remote sensing data were collected. We follow by discussing the observing strategy that was employed for the remote sensing data and providing a general description of the first results. This is followed by a more detailed analysis and an assessment of the overall accuracy for relating remote sensing observations to the derived physical characteristics. By creating accuracy models such as this, a trade space can be created for understanding the interplay of instrument characteristics with the desired accuracies for measuring the storage of carbon in the terrestrial biosphere.

Ecological research stations set in the temperate forests of the Northeastern United States such as the Harvard Forest in western Massachusetts, the Howland and Penobscott Forests in central Maine, or the Bartlett and Hubbard Brook Forests in New Hampshire serve as sites for studies in various topics related to forest ecology such as biodiversity, conservation, forest–atmosphere carbon exchange, and soil warming to name a few. Studies on forest biomass rely on these facilities as well; consequently, there is a historic legacy of documented efforts at these research forests dating as far back as the midtwentieth century [4]–[6]. In the summer of 2009, coordinated field campaigns focused on these sites to establish ground truth and calibrate remote sensing estimates of forest biomass, exploring the rationale for a potential spaceborne mission such as DESDynI. While measurements were made at other sites as well, this paper focuses only on the Harvard and Howland Forests. At each site, one-hectare plots measuring 200 m by 50 m (referred to as *hectares* throughout this paper) were laid out in regions of low-topographic relief. Each one of the hectares consisted of 16 smaller scale *subplots* measuring

Manuscript received July 23, 2012; revised November 12, 2012 and April 15, 2013; accepted June 29, 2013. Date of publication October 11, 2013; date of current version February 27, 2014. This research was conducted at the Jet Propulsion Laboratory, California Institute of Technology, under contract with the National Aeronautics and Space Administration.

R. Ahmed and S. Hensley are with the Jet Propulsion Laboratory, California Institute of Technology, Pasadena, CA 91109 USA (e-mail: razi.u.ahmed@jpl.nasa.gov).

P. Siqueira is with the Department of Electrical and Computer Engineering at the University of Massachusetts, Amherst, MA 01002 USA.

Digital Object Identifier 10.1109/TGRS.2013.2273738

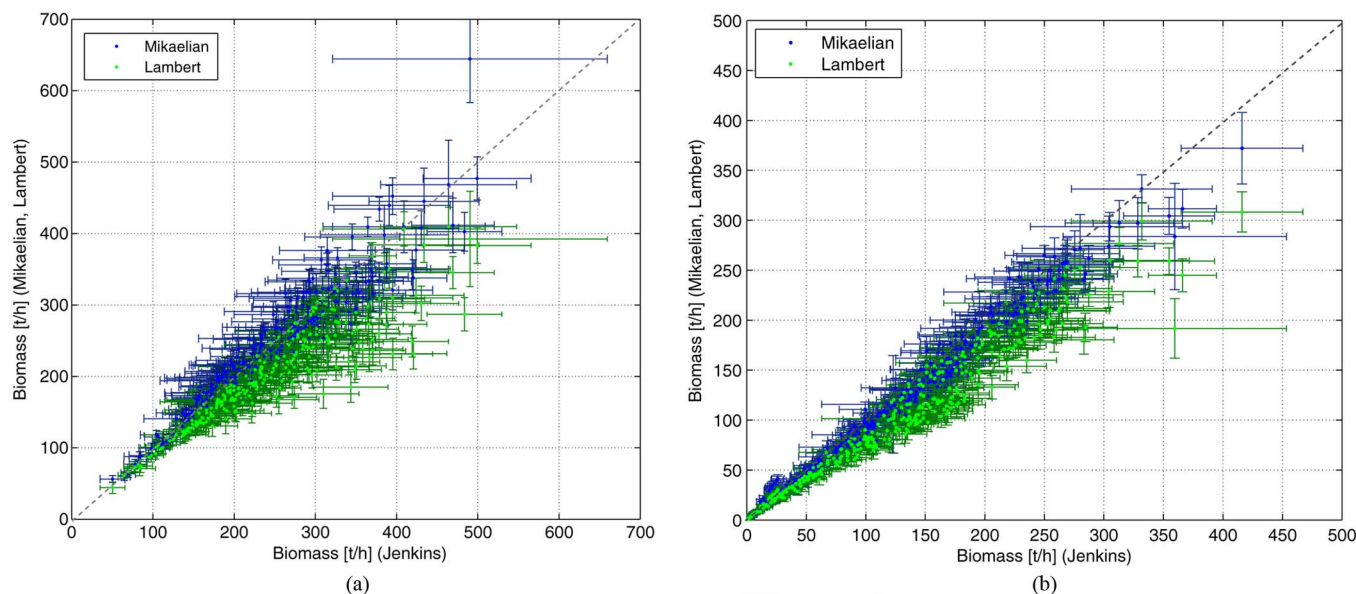


Fig. 1. Comparison of subplot-level biomass estimates in units of tons per hectare using the Mikaelian [8], Jenkins [9], and Lambert [10] allometries over the Harvard and Howland Forests. See [3] for explanation of methodology. (a) Harvard Forest. (b) Howland Forest.

25 m by 25 m. For each subplot, field data, such as species information and tree diameter (at breast height: dbh), were cataloged. The Harvard and Howland Forests are representative of the *Transition Hardwoods* of central New England [7], where trees predominantly belong to the Oak, Maple, Birch, Pine, and Hemlock families. Most of the trees measured at the two sites belonged to these five species. This per-tree species and diameter information from 15 hectares set in the Harvard Forest (split into four tracts, *Prospect Hill—PH*, *Slab City—SC*, *Tom Swamp—TS*, and *State Forest—SF*) and 23 hectares in the Howland (and the nearby Penobscott) Forests were aggregated over subplots and hectares to generate ground-truth estimates of forest biomass using allometric equations. A detailed account of the field campaigns, allometric equations, biomass estimates over these plots, and their associated accuracies can be found in [3]; however, a few results are reproduced here for convenience.

Three sets of allometric equations were used to estimate biomass from diameter data for plots set in both the Harvard and Howland Forests. The first set of equations is referred to in this paper as the Mikaelian equations, after work done by Michael Ter-Mikaelian [8] summarizing dbh–biomass allometric equations for 65 North American species from a number of studies conducted in research facilities such as the Harvard and Howland Forests. The second set of allometric equations is referred herein as the Jenkins equations after work done by Jennifer Jenkins [9] in developing ensemble diameter–biomass relationships from studies conducted across the continental United States. Finally, the third set of equations is referred to herein as the Lambert equations after work done by M. C. Lambert, C. H. Ung, and F. Raulier [10] publishing extensive allometric tables and associated errors using the ENFOR data set [11] across Canada.

Fig. 1 compares mean biomass for the 240 subplots at the Harvard Forest and 368 subplots at the Howland Forest estimated from the Jenkins allometry against subplot-level biomass estimates from the Mikaelian and Lambert equations for the

same subplots. The errors in biomass estimates from each of the allometries are shown as error bars of widths corresponding to 95% confidence intervals. Mean estimates from the Mikaelian and Jenkins equations are consistent while estimates from the Lambert equations are consistently lower. As there is no practical method for checking which estimate is closer to the true weight of the trees, therefore an analysis of all three allometries is presented. Subplot-level biomass estimates over the Harvard Forest range from 50 tons/ha to 500 tons/ha with mean values of roughly 200 tons/ha from Lambert and 250 tons/ha from the other two allometries. While the range of biomass values at the Howland Forest at subplot scales is similar to that of the Harvard Forest, there are, however, more subplots with fairly low-biomass values (less than 50 tons/ha) that are not present in the Harvard Forest data set.

Fig. 2 shows the per-tree estimates of weight aggregated for the corresponding plots to generate hectare-level biomass estimates from the three allometric equations over the Harvard and Howland Forests. Estimates of errors are shown as error bars using 95% confidence intervals. The biomass values for the 15 hectares over the Harvard Forest range from 115 to 350 tons/ha while the biomass estimates over the Howland (descriptor H) and Penobscott (descriptor P) range from close to zero (plot P9) to about 270 tons/ha (plot P1). The hectare-scale biomass estimates at Howland are not as high as those at the Harvard Forest primarily due to the larger number of hardwoods surveyed at the Harvard Forest; however, the low-biomass sites, such as P9 at Howland, are much lower than any found at the Harvard Forest, primarily because those are near clear-cut regions with very few small trees (about 77 trees in total with diameters ranging from 6 to 13 cm). Such sites were not surveyed at the Harvard Forest. The confidence intervals for these hectare-level biomass estimates are fairly narrow, with mean errors of 2 tons/ha for the Lambert and Mikaelian allometries and slightly higher errors of 4 tons/ha for estimates using the Jenkins allometry. There are significant differences between

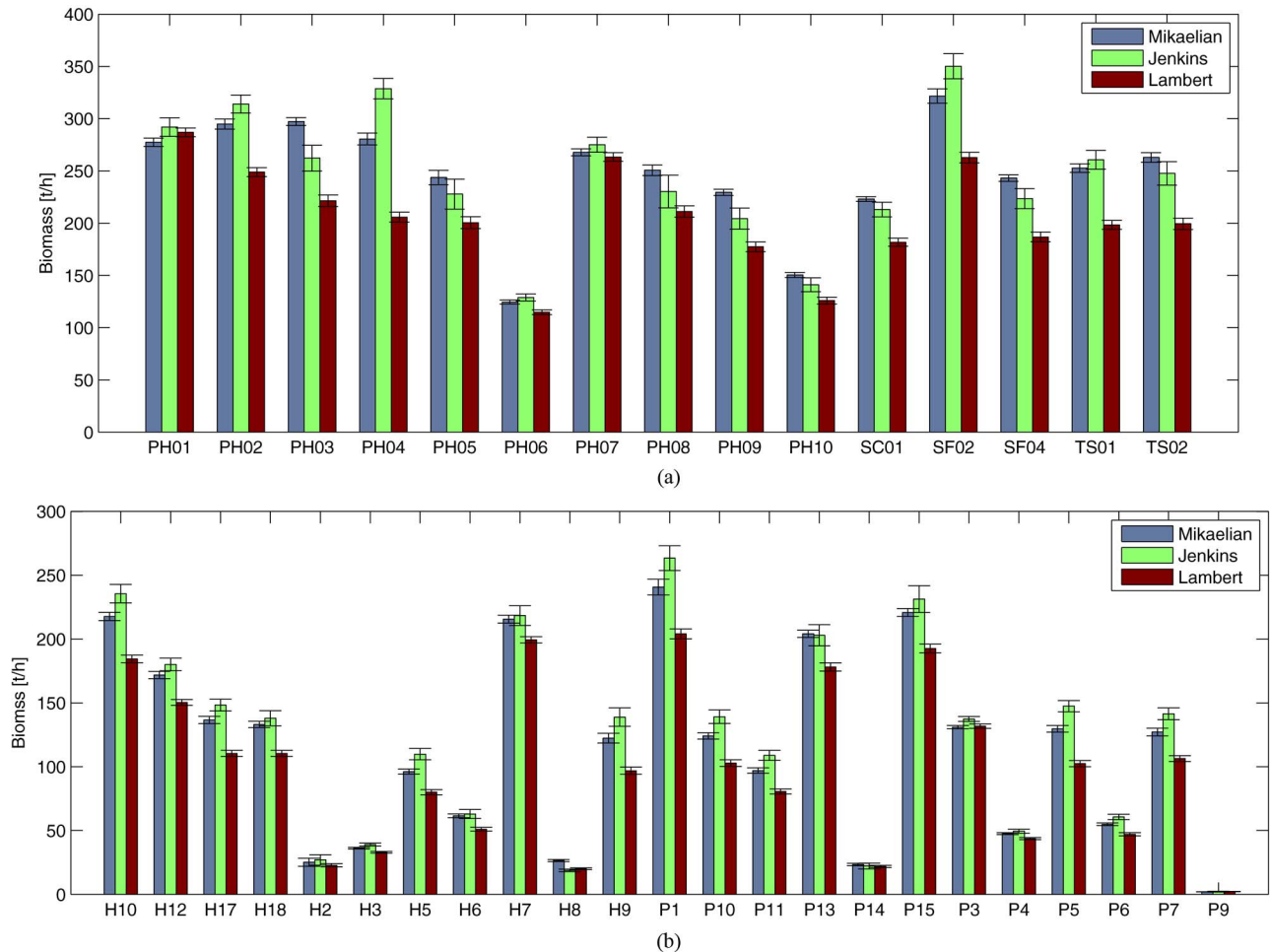


Fig. 2. Comparison of hectare-level biomass estimated using the Mikaelian [8], Jenkins [9], and Lambert [10] allometric equations over the Harvard and Howland Forests. See [3] for explanation of methodology. The naming convention for the Harvard Forest plots is based on the first two letters of the tracts (i.e., PH for Prospect Hill) followed by a unique number while that at the Howland Forest is a unique number following either an H for Howland or P for Penobscott. (a) Harvard Forest. (b) Howland Forest.

the mean biomass levels estimated from the three allometries at each plot. Short of weighing every tree individually, there are no means of establishing the true biomass at each site, so the relationship between backscatter and field biomass estimates is analyzed for each of the three allometries separately.

II. RADAR BACKSCATTER, ERROR MODEL, AND OBSERVATIONS

A backscattered radar signal consists of contributions from three major scattering mechanisms: 1) *single bounce*: from rough surfaces such as fields and water; 2) *double bounce*: from edges, such as those of buildings or tree trunks and the ground (named as such to indicate that the radar wave bounces twice before returning to the radar); and 3) *volumetric scattering*: from a diffuse object such as a canopy (with an arbitrary number of bounces). The backscattered signal is affected by each scattering mechanism depending on the nature of the scattering object, radar wavelength, polarization, and radar viewing geometry, among others. Polarimetric radars are capable of isolating the different scattering mechanisms for a particular target, for instance, the difference between like polarizations (HH–VV) tends to be dominated by double bounce, their sum (HH + VV) tends to be dominated by single-bounce scatterers,

and cross-polarization (HV) is mostly volumetric scattering. In closed canopy forests such as the Harvard and Howland Forests, volumetric scattering tends to be the dominant scattering mechanism for an L-band radar viewing at incidence angles larger than 30° . Since the intensity of backscatter from a volumetric target increases as the size of the volume increases, it is expected that cross-polarization data in such a configuration should be related to the size of the trees and, consequently, to their biomass. However, this is complicated by several factors, for instance, the loss of a signal's energy as it propagates through a canopy (known as signal extinction) reduces the intensity of volumetric backscatter, and while the extinction may be affected by factors such as moisture content in the canopy, those factors are not always related to the size of the volume. Furthermore, different tree species could have the same volumetric extent but different biomass levels because of their wood densities, complicating the simple backscatter to biomass inversion scenario.

A. Backscatter to Biomass

Regardless of the complications in relating forest biomass to radar backscatter, a large body of study exists where various backscatter and biomass relationships have been

developed and analyzed. In general, two types of approaches are adopted, one using radiative transfer models of radar scattering to parameterize radar backscatter as a function of the scattering volume [12], [13] (and by association biomass) and the other relying on purely empirical regression curves that exploit trends within the data alone [14], [15]. In the first case, the backscatter–biomass models invariably take the form of a power-law relationship, for instance, a study of the relationship between spaceborne imaging radar (L-band and C-band) and X-SAR (X-band) polarimetric data over sites in Northern Michigan [16] uses power-law relationships between polarimetric backscatter variables and structural elements of a forest such as basal area, tree heights, and crown and trunk biomass. Similarly, studies in the tropical forests [17], [18] or woodlands [19] using L- or C-band spaceborne synthetic aperture radar (SAR) imagery also relate radar backscatter and field biomass using power-law curves based on scattering models. While it is quite valuable to analyze the impact of different models on the backscatter–biomass relationship, something that has been extensively explored in the literature, it is not the intent of this paper. Here, we try to explore a more statistically rigorous approach for error analysis, and while it is mathematically convenient to adopt simpler regression models, we choose a model based on radar scattering so that the applicability of the framework is not limited to this data set. The backscatter–biomass model used here has been adapted from [20] and [21] and is given by

$$\sigma = \beta_0(1 - e^{-\beta_1 M}) + \beta_2 M^\alpha e^{-\beta_1 M} \quad (1)$$

where σ is the radar backscatter, M is the biomass, and α , an empirically determined factor, is fixed to 0.2. This model will be used throughout the analysis presented here to ascertain the uncertainty in biomass estimates from radar backscatter.

B. Error in Radar Estimates of Biomass

The set of coefficients, $\beta = [\beta_0, \beta_1, \beta_2]$, in (1) is generally obtained for a particular field site using nonlinear regressions between radar data and corresponding field estimates of biomass. In regression analysis, the accuracy of estimates is often characterized by confidence and prediction intervals. To see how these bounds can be developed for biomass estimates from radar backscatter, we consider first a general nonlinear-regression scenario, where a variable \mathbf{Y} is related to a set of variables given by \mathbf{X} such that

$$\mathbf{Y} = f(\beta, \mathbf{X}) + \epsilon \quad (2)$$

where \mathbf{Y} is an $n \times 1$ vector, referred to as the *response*, while \mathbf{X} is an $n \times k$ matrix of n measurements from k predictors. The set of coefficients, β , is a $p \times 1$ dimensional vector (for p coefficients) while $\epsilon = (\epsilon_1, \dots, \epsilon_n)$ is referred to as the *error in equation* or *model error*. The confidence interval on estimates of \mathbf{Y} for the estimated set of coefficients, $\hat{\beta}$, is given by

$$\hat{y}_i \pm t_{\alpha/2} \sqrt{S_{y_i}^2} \quad (3)$$

where $t_{\alpha/2}$ is the $\alpha/2$ upper critical value for the standard normal distribution (for instance, at a significance level of 95%, $t_{\alpha/2} = 1.96$), while S_{y_i} , the standard error for the i th response, \hat{y}_i , can be estimated using the *delta* method, given by [22]

$$S_{y_i}^2 = \mathbf{F}'_{\beta} \hat{\Sigma}_{\beta} \mathbf{F}_{\beta} \quad (4)$$

where $\hat{\Sigma}_{\beta}$ is the covariance matrix of the regression coefficients and the vector \mathbf{F}_{β} is a set of partial derivatives of the model function with respect to the coefficients, $\hat{\beta}$, such that

$$\mathbf{F}_{\beta} = \left[\frac{\partial f}{\partial \beta_1}, \dots, \frac{\partial f}{\partial \beta_p} \right]^T \quad (5)$$

The covariance matrix $\hat{\Sigma}_{\beta}$ is estimated by [23]

$$\hat{\Sigma}_{\beta} = (\mathbf{J}^T \mathbf{J})^{-1} \quad (6)$$

where \mathbf{J} , sometimes referred to as the Jacobian, is an $n \times p$ matrix constructed such that each row is the vector \mathbf{F}_{β}^T evaluated at \mathbf{X}_i for $i = 1, \dots, n$. Similarly, a prediction interval is estimated by

$$\hat{y}_i \pm t_{\alpha/2} \sqrt{S_{y_i}^2 + \hat{\sigma}^2} \quad (7)$$

where $\hat{\sigma}^2$ is the variance of the error in equation, given in vector form as ϵ .

In the backscatter–biomass regression scenario, the nonlinear relationship between the observed backscatter and estimated biomass is given in (1). Since this equation describes a *forward model*, the backscatter coefficient σ is the response (\mathbf{Y}) while biomass M is the sole predictor (\mathbf{X}) for n measurements with $k = 1$, with $p = 3$ for three coefficients $\beta_0, \beta_1, \beta_2$ (α is considered to be a constant for this analysis). Confidence and prediction intervals, from (3) and (7), would then characterize the uncertainty of the estimated backscattering coefficient. These intervals would have to be numerically inverted to obtain the uncertainties in biomass estimates. A numerical inversion is unavoidable since a closed-form solution to (1) does not exist.

C. Accounting for Parametric Measurement Error

The calculation of confidence intervals described in (3) and (7) does not include a treatment of measurement errors. If there are errors in measuring the response and the predictor (in this case, backscatter and biomass, respectively), the uncertainty in biomass estimates should be effected when those error-prone measurements are used to estimate the coefficients in the first place. In a general nonlinear-regression scenario with *additive* measurement error, the terminology changes to include errors in both the predictor \mathbf{X} and the response \mathbf{Y} . Borrowing the terminology from [22] and [24], the error-prone measurement of the response \mathbf{Y} is denoted by \mathbf{D} such that

$$D_i = y_i + q_i \quad (8)$$

where q_i is the error in the measurement of response (i.e., the backscatter) such that $E(q_i | y_i, \mathbf{x}_i) = 0$ and

$Var(q_i|y_i, \mathbf{x}_i) = \sigma_{qi}^2$. Similarly, an error-prone measurement of the predictor (the biomass) \mathbf{X} is given by \mathbf{W} such that

$$\mathbf{W}_i = \mathbf{x}_i + \mathbf{u}_i, \quad i = 1, \dots, n \quad (9)$$

where \mathbf{u}_i is a vector of the error in the measurement of the predictors with $E(\mathbf{u}_i|y_i, \mathbf{x}_i) = 0$, $Cov(\mathbf{u}_i|y_i, \mathbf{x}_i) = \Sigma_{ui}$, and $Cov(\mathbf{u}_i, q_i|y_i, \mathbf{x}_i) = \Sigma_{uqi}$. The covariance matrix Σ_{ui} (the covariance of errors in the measurement of \mathbf{X}_i , the predictors) is a $k \times k$ matrix while Σ_{uqi} is the covariance between the errors in the predictor and response. Since there is no practical reason for errors in the measurement of backscatter and biomass to be related, Σ_{uqi} is ignored here by setting it to zero. Finally, the relationship used in the nonlinear-regression algorithms is given by

$$\mathbf{D} = f(\beta, \mathbf{W}) + \epsilon \quad (10)$$

where the error in equation, ϵ , remains the same $n \times 1$ vector with variance $\hat{\sigma}^2$. The calculation of confidence and prediction intervals is still the same as described in (3) and (7); however, the estimation of the covariance matrix $\hat{\Sigma}_\beta$ is no longer as simple as given in (6). The covariance matrix must now account for three more error sources, namely, q_i , the error in response, \mathbf{u}_i , the error in predictors, and the covariance of the two errors Σ_{uqi} . This problem is simpler in a linear-regression scenario, where equations have been developed that allow for the estimation of the covariance matrix with additive measurement error [22]. The case of nonlinear regressions is, however, much more complicated. There is no one method for estimating the covariance matrix Σ_β in a nonlinear-regression setting with measurement error in both the response and predictor. An analytical solution in such a case has to be tailored to the particular model function. While such an analysis could be conducted for the backscatter–biomass case, doing so would require much deeper insight into the nuances of statistics, and although that would be of some academic value, it is avoided here for simplicity.

The most common work-around is to use simulation or Monte Carlo-type techniques. The problem is twofold: The first is to correct the bias in coefficients β introduced by measurement error, and the second is to estimate the covariance matrix itself. The solution to the first problem is handled by the method called simulation and extrapolation (SIMEX) [25], while the second is handled by the *bootstrap* [22].

1) *Parametric Bootstrapping*: The more common form of the bootstrap, called the *one-stage bootstrap*, estimates the statistics of the data, such as the variance, by using different or all possible combinations of the data (with or without replacing samples). Such a method is useful as it makes no assumptions about the statistics of the error. It does, however, lack the ability to assess the impact of noise that may not be present in that particular data set, limiting its usefulness when an analysis of the measurement errors is required. Parametric bootstrap, or a *two-stage bootstrap*, on the other hand, simulates a large number of data sets using realizations of measurement errors with the intent of relying on sample statistics to estimate standard errors

and, thus, the confidence intervals. A description of the method follows.

Given a set of predictors \mathbf{W}_i (in this case, simply biomass) and an estimate of their error variances $\hat{\sigma}_{ui}^2$, we construct a large number of imperfectly measured predictors such that [22]

$$\mathbf{W}_{bi} = \mathbf{W}_i + \mathbf{u}_{bi} \quad i = 1, \dots, n \quad (11)$$

where $\mathbf{u}_{bi} \sim N(0, \hat{\sigma}_{ui}^2)$ for $b = 1, \dots, B$, where B is the number of bootstrap realizations and should be large. If the number of predictors were larger than one, then $\hat{\sigma}_{ui}^2$ is replaced with $\hat{\Sigma}_{ui}$ which requires knowledge of not just the variance but also the covariances between the errors in measuring the predictors. The response without any measurement error but with an error in equation (the model error) is then calculated such that [22]

$$Y_{bi} = f(\hat{\beta}_c, \mathbf{W}_{bi}) + \epsilon_b \quad i = 1, \dots, n \quad (12)$$

where $\hat{\beta}_c$ denotes unbiased coefficients (obtained using SIMEX, which is to be described later) and $\epsilon_{bi} \sim N(0, \hat{\sigma}^2)$. The error-prone measurement of the response is then calculated using [22]

$$D_{bi} = Y_{bi} + q_{bi} \quad i = 1, \dots, n \quad (13)$$

where $q_{bi} \sim N(0, \hat{\sigma}_{qi}^2)$ and $\hat{\sigma}_{qi}^2$ is the estimate of variance of the measurement error in the response (in this case, backscatter). For each bootstrap sample, a set of coefficients $\hat{\beta}_b$ is estimated using nonlinear fits between \mathbf{D}_b and \mathbf{W}_b . Finally, the covariance matrix $\hat{\Sigma}_\beta$ is estimated by computing the sample covariance of the coefficients $\hat{\beta}_b$ for $b = 1, \dots, B$.

The implementation of this method is complicated by problems of nonconvergence of the nonlinear fitting algorithms. Often, convergence relies on a good initial guess, which is not easy to automate. Since the number of bootstrap samples, B , needs to be large enough to have meaningful estimates of the covariance matrix, nonconvergence could potentially make the problem of estimating the confidence intervals impossibly hard. Furthermore, obtaining information about the variance of the error in equation, $\hat{\sigma}^2$, is not simple. This quantity is generally not known *a priori*, certainly not in the backscatter–biomass case. While it is logical to use the mean squared residuals from the fit as an estimate, the residuals tend to be contaminated by measurement error in both the response and the predictor [22]. An estimate of the variance of ϵ would thus require removing, or deconvolving, the effects of measurement error from the residuals. This is often quite complicated and model dependent. An approximate solution can be borrowed from linear regression, given by [22]

$$\hat{\sigma}^2 = \frac{\sum_i (D_i - f(\hat{\beta}_c, \mathbf{W}_i))^2}{n - k} - \hat{\sigma}_q^2 - \mathbf{F}_X^T \hat{\Sigma}_u \mathbf{F}_X \quad (14)$$

where

$$\hat{\sigma}_q^2 = \sum_i \frac{\sigma_{qi}^2}{n}, \quad \hat{\Sigma}_u = \sum_i \frac{\hat{\Sigma}_{ui}}{n} \quad (15)$$

$$\mathbf{F}_X = \left[\frac{\partial f}{\partial X_1}, \dots, \frac{\partial f}{\partial X_k} \right]^T. \quad (16)$$

In the backscatter–biomass case of (1), since \mathbf{X} is simply M , therefore, \mathbf{F}_X reduces to a scalar, $\mathbf{F}_X = \partial f / \partial M$. In essence, the use of (14) through (16) has the effect of subtracting estimates of measurement error from the fit residuals to approximate the model error or error in equation.

2) *SIMEX: Simulation Extrapolation*: The introduction of measurement error in both the response and predictor biases the estimated regression coefficients [22]. The SIMEX method attempts to estimate the amount of bias caused by error in the measurement of \mathbf{X} and \mathbf{Y} [25]. These unbiased coefficients are needed for the bootstrap procedure described earlier. Essentially, SIMEX assesses the trend in coefficients as a function of measurement error. Mathematically, it postulates that $\beta_j(\lambda)$ for $j = 1, \dots, p$ (for p coefficients) is unbiased for $\lambda = -1$ if the covariance matrix of the measurement errors of the predictors is given by $Cov(\mathbf{u}_i) = (1 + \lambda)\mathbf{\Sigma}_{ui}$ instead of $\mathbf{\Sigma}_{ui}$ and the variance of the measurement error of the response is given by $(1 + \lambda)\hat{\sigma}_{qi}^2$ rather than $\hat{\sigma}_{qi}^2$. The procedure for computing $\beta_j(\lambda)$ at $\lambda = -1$ is similar to the bootstrap itself. Here, for each λ , SIMEX predictors with known covariances are calculated such that [22]

$$\mathbf{W}_{si}(\lambda) = \mathbf{W}_i + \lambda^{1/2}\mathbf{u}_{si} \quad i = 1, \dots, n \quad (17)$$

for $s = 1, \dots, S$ (for large values of S) with $Cov(\mathbf{u}_i) = \mathbf{\Sigma}_{ui}$. Similarly, the error in response is added for each λ to calculate the SIMEX $D_{si}(\lambda)$ such that

$$D_{si}(\lambda) = D_i + \lambda^{1/2}q_{si} \quad i = 1, \dots, n. \quad (18)$$

Coefficients $\hat{\beta}_s(\lambda)$ are estimated for each SIMEX sample and averaged to calculate

$$\hat{\beta}(\lambda) = \sum_s \frac{\hat{\beta}_s(\lambda)}{S}. \quad (19)$$

Typically, second-order quadratic polynomials are fitted to each of the coefficients, $\beta_j(\lambda_s)$, and the unbiased estimate of $\hat{\beta}$ is obtained by evaluating those polynomials at $\lambda = -1$ [25], [22].

The parametric bootstrap and SIMEX comprise a mathematical framework where errors in measurements of biomass and backscatter can be included in an assessment of the accuracy of biomass estimates from radar backscatter. The errors in measurements of biomass at the Howland and Harvard Forests were characterized earlier, and a description of the errors in measuring backscatter follows.

D. Backscatter Error Model

Uncertainties in radar measurements are a consequence of the random nature of the scattering process and the noise within a radar instrument itself (e.g., thermal noise, imaging ambiguities, etc.). The contributors to what would amount as error in a radar backscatter measurement when biomass estimation is of interest include, among others, image speckle, calibration errors, topographic effects, and variability due to changes such as soil moisture. The contribution of each error source to the

total error budget depends on a slew of factors ranging from systematic instrument parameters to weather conditions. To be able to inform the framework laid out in previous sections regarding error in biomass estimation from radar, a thorough accounting of the radar backscatter error budget is in order. While a complete description of the radar error model used in this paper can be found in [21] and [20], a brief discussion of the error terms follows. The total error in backscatter, $\Delta\sigma$, is modeled as a sum of four major error sources

$$\Delta\sigma = \Delta\sigma_s + \Delta\sigma_t + \Delta\sigma_c + \Delta\sigma_a \quad (20)$$

where $\Delta\sigma_s$ captures the effect of image speckle and thermal and multiplicative noise, $\Delta\sigma_t$ describes the temporal variation in radar backscatter unrelated to biomass change, $\Delta\sigma_c$ is the error in backscatter calibration, and $\Delta\sigma_a$ is the error in backscatter due to incorrect area projection normalization.

1) *Image Speckle and Thermal and Multiplicative Noise*: The first term in (20), $\Delta\sigma_s$, combines the effect of image speckle (due to the coherent nature of radar scattering), thermal noise, and sources of multiplicative noise such as ambiguities, impulse response sidelobes, and quantization noise. This term is modeled in [21] as a modified version of the scatterometer error equation, given by

$$\Delta\sigma_s = \frac{1}{\sqrt{N}} \left(\frac{1}{\sqrt{N_{os}}} + \frac{1}{\sqrt{N_{ot}}} \frac{1 + \text{SNR}/\text{MNR}}{\text{SNR}} \right) \sigma \quad (21)$$

where N is the number of spatial looks or averages, while N_{ot} is the total number of repeat observations as the sum of speckle identical N_{oi} and speckle diverse N_{os} observations, $N_{ot} = N_{os} + N_{oi}$, where this distinction is introduced to account for observations from slightly different observation geometries where speckle is correlated (speckle identical) such as in interferometry and observation geometries that are very dissimilar and where speckle is uncorrelated (speckle diverse) such as from ascending and descending passes of a satellite. The variable SNR in (21) refers to the signal-to-noise ratio from thermal noise only while MNR is the multiplicative-noise ratio often due to observation errors such as range and azimuth ambiguities. The number of spatial looks, N , can be computed for an imaged area using

$$N = \frac{A_g \sin \theta_i}{\kappa_\rho \Delta\rho \kappa_s \Delta s} \quad (22)$$

where A_g is the area of the region over which image pixels are spatially averaged (for example, the area of the field sites where biomass is estimated), θ_i is the local incidence angle, $\Delta\rho$ and Δs are the range and the azimuth resolution (or spacing), respectively, and κ_ρ and κ_s are the broadening factors in range and azimuth, accounting for the loss of resolution due to the use of windowing in the image formation process. The range resolution is given by

$$\Delta\rho = \frac{c}{2B} \quad (23)$$

where c is the speed of light and B is the signal bandwidth. The maximum azimuth resolution Δs for a synthetic aperture system is given by

$$\Delta s = \frac{L_{az}}{2} \quad (24)$$

where L_{az} is the azimuth dimension of the antenna. The broadening factors, κ_ρ and κ_s , can be approximated by

$$\kappa_{\rho,s} \approx 1.6363 - 0.6363\sqrt{\eta} \quad (25)$$

where the parameter η depends on the type of windowing employed during the compression of the range or azimuth spectra, for instance, $\eta = 1$ corresponds to uniform weighting, $\eta = 0$ corresponds to the Hanning window, $\eta = 0.08$ corresponds to the Hamming window, etc. The SNR is given by

$$\text{SNR} = \frac{\sigma}{\bar{\sigma}_0} \quad (26)$$

where σ is the backscatter value and $\bar{\sigma}_0$ is the system-specific noise equivalent backscatter coefficient. The MNR is given by

$$\frac{1}{\text{MNR}} = \text{ISLR}_\rho + \text{ISLR}_s + \frac{1}{\text{AMB}_t} + \frac{1}{\text{QNR}} \quad (27)$$

where ISLR_ρ and ISLR_s are the integrated sidelobe ratios in range and azimuth for sidelobes arising from the range and azimuth compression techniques associated with a pulse compression SAR system. AMB_t is the total signal-to-ambiguity ratio (including the effect of both range and azimuth ambiguities), referring to the ambiguities that arise from the uncertainty in associating a backscattered radar signal with its corresponding transmitted signal. The quantization-noise ratio (QNR), a ratio of the signal power to the quantization-noise power, is dependent on the quantization scheme but can be approximated by [26]

$$\text{QNR} \approx 2.0 + 6.02b \quad (28)$$

for QNR expressed in decibels and b referring to the number of bits used in quantization. The integrated sidelobe ratios, ISLR_ρ and ISLR_s , are essentially the ratios of the total energy in the sidelobes to the energy in the main lobe of a compressed range or azimuth signal. These ratios are dependent on the type of window used in the image formation process; however, they are approximated by polynomial fits to numerical evaluations of the energy integrals as a function of the broadening factor η as [21]

$$\text{ISLR}_{\rho,s}(\eta) = -46.965 + 104.11\eta - 112.59\eta^2 + 43.124\eta^3 \quad (29)$$

with the ISLR expressed in decibels and η being the same window-specific parameter described earlier.

2) *Temporal Variation*: Temporal variability in radar backscatter, given by the variable $\Delta\sigma_t$ in (20), can, in principle, encompass effects from many physical processes such as weather, anthropogenic changes, etc. Although change in forest biomass may also affect radar backscatter, that change would not be considered an error but rather an observation. Here, temporal variation refers to changes in backscatter from one

observation to another from all processes that have no impact on forest biomass. It is difficult to have a generic model that explains temporal variation for all possible scenarios; as a result, this error is invariably treated differently from one data set to another.

3) *Error in Backscatter Calibration*: The sampled radar signal, a unitless digital number ranging from 0 to $2^b - 1$ for a b -bit digitizer, is converted to physical units by normalizing that number by a calibration constant. The calibration error term $\Delta\sigma_c$ refers to the errors introduced by unknowns in the computation of the calibration constant. Systematic calibration errors arise from uncertainties in pointing and geolocation, while random errors arise from the uncalibrated behavior of radar electronics. The calibration error is modeled in [21] as

$$\Delta\sigma_c = \frac{1}{\sqrt{N_{ot}}} \Delta\sigma_{ran} + \frac{1}{\sqrt{N_{ot}}} \Delta\sigma_p + \frac{1}{\sqrt{N_{os}}} \frac{1}{\sqrt{N}} \sqrt{\frac{A_{dem}}{A_{pix}}} \Delta\sigma_{geo} \quad (30)$$

where $\Delta\sigma_{ran}$ denotes the random errors from the uncalibrated behavior of the electronics, $\Delta\sigma_p$ denotes the errors in calibration due to pointing uncertainty, and $\Delta\sigma_{geo}$ denotes the error due to inaccuracies of the digital elevation model (DEM) used for orthorectification, while A_{pix} and A_{dem} are the areas of the image and DEM pixels, respectively. Since pointing and random calibration errors tend to be correlated for a particular scene, they are unaffected by spatial averaging and are thus modeled without any dependence on N . The random calibration error term $\Delta\sigma_{ran}$ captures the effect of uncertainty in estimating the instrument gain needed to compute the calibration constant. It is calculated from an instrument-specific residual random calibration term, $\Delta\sigma_{dB}$ (specified in decibels), by

$$\Delta\sigma_{ran} = \sigma_t(10^{\Delta\sigma_{dB}/10} - 1) \quad (31)$$

where σ_t is the true backscatter. The effects of antenna patterns on radar backscatter are usually removed through calibration by using measured antenna patterns and an estimate of the antenna pointing direction. Uncertainties in the antenna pointing result in an incorrect compensation of the backscatter and, therefore, error in a backscatter measurement of biomass, denoted by $\Delta\sigma_p$. This error term would depend on the antenna patterns themselves. This error, however, can be approximated by assuming a two-way *sinc* pattern for the antenna gain such that

$$\Delta\sigma_p \approx -\sigma \left(\frac{\Delta G_{r,\rho}}{G_{r,\rho}} + \frac{\Delta G_{r,s}}{G_{r,s}} + \frac{\Delta G_{t,\rho}}{G_{t,\rho}} + \frac{\Delta G_{t,s}}{G_{t,s}} \right) \quad (32)$$

where $G_{x,y}$ refers to the transmit and receive (t, r) gain compensation in range and azimuth (ρ, s). Using global averaged values of the gain compensation term, the relative gain error in the range direction is given as a function of the pointing error $\Delta\theta$ as

$$\frac{\Delta G_{x,\rho}}{G_{x,\rho}} = \frac{4\Delta\theta}{\theta_{1/2}} \ln \left[\text{sinc} \left(\frac{\pi}{2k} \right) \right] \quad (33)$$

where $\theta_{1/2}$ is the elevation half-power beamwidth and k is a beam shaping factor (assumed to be 1.136 for a uniformly

weighted array; a common configuration). Similarly, the relative gain error in the azimuth direction is given by

$$\frac{\Delta G_{x,s}}{G_{x,s}} = \frac{2k\Delta\theta}{\pi} \left(\frac{\ln[\text{sinc}(\pi/2k)]}{\int_0^{\pi/2k} \text{sinc}^2(x)dx} \right). \quad (34)$$

Finally, the geolocation error $\Delta\sigma_{geo}$ arising from errors in the DEM that cause errors in estimating the radar pointing direction and, therefore, an incorrect antenna gain calibration is calculated from (33) with the pointing error given by

$$\Delta\theta = \frac{\Delta h_{dem}}{\rho} \quad (35)$$

where Δh_{dem} is the height accuracy of the DEM and ρ is the range.

4) *Errors Due to Pixel Area Normalization:* In a calibrated radar, the radar cross section is normalized to the scattering area to calculate the radar backscattering coefficient σ . Ground topography can have a significant impact on the scattering area and, therefore, the backscatter coefficient. To estimate biomass, topographic effects in backscatter must be accounted for in the processing chain. However, uncertainties in the ground topography introduce error in the corrected backscatter. This effect is captured in the term $\Delta\sigma_a$ in (20) and is modeled in [21] as

$$\Delta\sigma_a = \frac{1}{\sqrt{N_{os}}} \sqrt{\frac{A_{dem}}{A_{pix}}} \frac{1}{\sqrt{N}} \left(\frac{\Delta A_c}{A_c} \right) \sigma \quad (36)$$

where the relative area projection error $\Delta A_c/A_c$, a function of the DEM height error Δh_{dem} , is given by

$$\frac{\Delta A_c}{A_c} = \frac{\sin(2\tau_\rho) \sin^2(\tau_s) + \sin(2\tau_s) \sin^2(\tau_\rho)}{2 - 2 \sin^2(\tau_\rho) \sin^2(\tau_s)} \Delta\tau + \frac{\cos(\theta - \tau_\rho - \tau_s)}{\sin(\theta - \tau_\rho) \cos(\tau_s)} \Delta\tau \quad (37)$$

where τ_ρ and τ_s are the mean slopes in the range and the azimuth direction for incidence angle θ , while $\Delta\tau$ is the error in determining the range or azimuth slopes (considered to be the same here), given by

$$\Delta\tau = \frac{\Delta h_{dem}}{L_{dem} (1 + \tan^2(\tau_x))} \quad (38)$$

where Δh_{dem} is the DEM height error, L_{dem} is the DEM posting, and τ_x is the slope in either the range or azimuth direction.

E. Radar Measurements

During the summer of 2009, in conjunction with the field campaigns, NASA JPL's UAVSAR [27] was flown over the Harvard and Howland Forest regions. The flightlines were designed to be in a racetrack configuration so that the left looking antenna could image the same area from two different aspect angles (by flying at opposite headings, hence the term racetrack). At the Harvard Forest, UAVSAR collected a total of 40 scenes on five days, the 6th, 8th, 13th, 16th, and 17th of August, with 20 scenes from each heading of 5° and 185° . At the Howland Forest, UAVSAR was flown at headings of 167° and 347° collecting ten scenes at each heading on three

TABLE I
UAVSAR INSTRUMENT PARAMETERS

Parameter	Value
Frequency	1.26GHz
Bandwidth	80MHz
Polarization	HH, HV, VH, VV
Look Angles	$25^\circ - 65^\circ$
Swath Width	16km
Resolution	$1.6m \times 0.66m$

days, the 5th, 7th, and 14th of August. Table I lists some key parameters of the UAVSAR instrument.

UAVSAR data are distributed by NASA/JPL either in the slant-range geometry or as ground-projected images using the 30-m resolution Shuttle Radar Topography Mission (SRTM) DEM for orthorectification. In either format, the antenna pattern artifacts are removed in calibration by using precise antenna models and best estimates of the pointing angle. The two artifacts that do remain in the distributed data are due to pixel area effects from topographic variations and the dependence of radar backscatter on the incidence angle [28], [29]. Before UAVSAR backscatter data can be used to estimate biomass, both these artifacts must be removed [30].

Topographic variations cause the area of imaged pixels to be projected differently in the radar look direction. This variation causes the backscattering coefficient, which is normalized to the scattering area, to vary with topography. For the UAVSAR data used in this analysis, topographic artifacts are removed using the algorithm outlined in [31], where the corrected backscatter coefficient σ_{pix} is given by

$$\sigma_{pix} = \sigma \cos \psi \quad (39)$$

where σ is the calibrated ground-projected backscatter coefficient (as distributed by NASA/JPL) and the projection angle ψ is given by

$$\cos \psi = \hat{n} \cdot (\hat{x} \times \hat{R}) \quad (40)$$

where \hat{n} is the unit surface normal, \hat{x} is the unit vector in the along-track direction, and \hat{R} is the unit look vector. The surface normal is computed from the resampled coregistered 30-m SRTM DEM that is distributed with the UAVSAR data, while the look vector is computed from UAVSAR peg parameters [32]. The second artifact, that of the dependence of volume backscatter on the incidence angle, or the backscatter law, is compensated by [29], [28]

$$\sigma_{inc} = \sigma_{pix} \left(\frac{\cos \theta}{\cos \theta_i} \right) \quad (41)$$

where θ is the reference incidence angle (where no correction is applied) while θ_i is the local incidence angle, given by [31]

$$\cos \theta_i = \hat{n} \cdot \hat{R} \quad (42)$$

where \hat{n} and \hat{R} are the unit surface normal and look vectors described before. While the pixel area correction is valid everywhere, the backscatter law in (41) is only valid over forested regions since it relies on an assumption of the trend in volume backscatter as a cosine of the local incidence angle. This trend

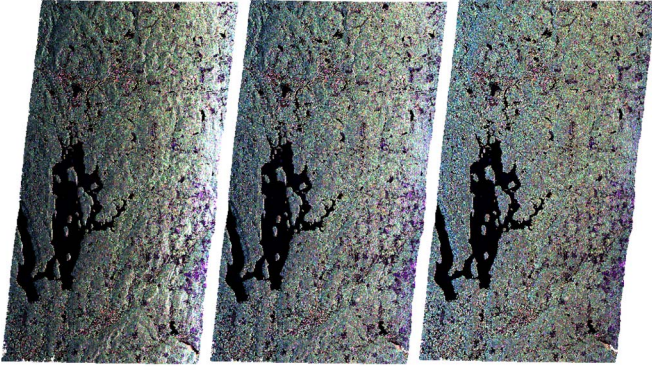


Fig. 3. Polarimetric composite (HH—red, HV—green, VV—blue) of three stages of the UAVSAR backscatter correction. The left plane shows the calibrated image distributed by JPL, the center image is corrected for pixel area variations, and the image on the right is corrected for both the pixel area variations and the backscatter law.

TABLE II
LIST OF UAVSAR SCENES CHOSEN OVER THE
HARVARD AND HOWLAND FORESTS

Harvard Forest			Howland Forest		
Line	Flight	Date	Line	Flight	Date
00502	09057-001	08/08/09	16701	09054-008	08/05/09
00502	09065-005	08/17/09	16701	09054-010	08/05/09
00503	09057-003	08/08/09	16701	09056-008	08/07/09
00505	09057-005	08/08/09	16701	09056-012	08/07/09
00506	09065-007	08/17/09	16701	09061-008	08/14/09
00508	09060-000	08/13/09	16701	09061-010	08/14/09
00509	09057-007	08/08/09	16702	09054-012	08/05/09
00509	09060-002	08/13/09	16702	09054-014	08/05/09
00512	09065-003	08/17/09	16702	09054-016	08/05/09
00513	09065-001	08/17/09	16702	09056-014	08/07/09

is not valid for all scattering mechanisms. Fig. 3 shows the two corrections applied to one of the scenes acquired at a heading of 5° over the Harvard Forest. The leftmost image is the calibrated ground-projected image distributed by JPL. The variation in backscatter intensity as a result of pixel area and incidence angle variation across the swath is quite apparent. The center image has been corrected for pixel area variations due to topography, given by (39). The effect of this correction is visible as a decrease in backscatter intensity from hills facing the radar as well as a reduction of the cross-swath trend in backscatter. The rightmost image in Fig. 3 has been corrected for the backscatter law using (41) as well as pixel area variations. As expected (and desired), almost all topographic and cross-swath trends are visibly absent from this image. There are, however, some trends in the polarimetric composition, evident by the dominance of the blue component, representing the VV-channel, at father ranges. Since the backscatter law assumed for this analysis is independent of polarization, this trend is expected [29].

Table II lists the identifiers for ten UAVSAR scenes chosen for analyzing the backscatter–biomass relationship over the Harvard and Howland Forests. The acquisition date for each scene is also listed. All of these scenes are corrected for pixel area and the backscatter law, as described earlier. The UAVSAR orthorectified imagery is distributed in the equiangular projection using the WGS84 ellipsoid with equal pixel spacing of $5.556 \times 10^{-5}^\circ$ (approximately 6.2 m in the E/W direction and 4.5 m in the N/S direction). Pixels corresponding to a particular

field site are chosen from the imagery based on the amount of overlap between a pixel and its corresponding ground site. An analysis of the backscatter–biomass relationship over the Harvard and Howland Forests using these scenes follows.

III. RESULTS AND DISCUSSION

With field estimates of biomass and backscatter intensity data from UAVSAR collected at approximately the same time, this data set allows for a ready analysis of the relationship between radar backscatter and biomass in the temperate forests of the Northeastern United States. Although a framework has been established that allows for an analysis of errors in biomass estimates from backscatter in the presence of measurement error in both backscatter and field biomass, it is instructive to look at biomass uncertainty without considering measurement error first.

A. Harvard Forest

Figs. 4–6 plot the subplot and hectare-scale field estimates of biomass obtained from the three different allometries Mikaelian [8], Jenkins [9], and Lambert [10] against average cross-polarized (HV) backscatter data from the ten UAVSAR scenes listed in Table II over the 240 subplots and 15 hectares at the Harvard Forest. The backscatter, plotted at the subplots or the hectare scales, is estimated by averaging ground-projected UAVSAR pixels such that

$$\bar{\sigma} = \frac{1}{N} \frac{1}{N_{ot}} \sum_p^N \sum_q^{N_{ot}} \sigma_{pq} \quad (43)$$

where N is the number of spatial looks and N_{ot} is the number of repeat observations of the single-look backscatter σ_{pq} . Since the backscatter data plotted here are chosen from the ground-projected imagery which is already spatially multilooked, the number of ground-projected pixels averaged is not the same as the number of looks, N , given by (22). Since the incidence angle at the Harvard Forest for all the scenes was designed to be around 40° , the number of looks, N , for subplots of area $25 \text{ m} \times 25 \text{ m}$, with a native UAVSAR single-look resolution of $1.6 \text{ m} \times 0.66 \text{ m}$ and broadening factors of 1.45 in range and azimuth (for a Hamming window), is approximately 187, while at hectare scales, $N \approx 2790$. The ten scenes from the lines listed in Table II were all collected from almost the same look geometry (for repeat-pass interferometry), and they are considered to be speckle identical; therefore, here $N_{ot} = N_{oi} = 10$. The confidence and prediction intervals are calculated from (3) and (7), respectively, with $t_{\alpha/2} = 1.96$. The covariance matrix of coefficients, $\hat{\Sigma}_\beta$, is estimated from (6) while the error in equation, needed for calculating the prediction intervals, is estimated from mean square residuals of the nonlinear fit to the backscatter–biomass forward model given in (1).

B. Howland Forest

Figs. 7–9 plot field biomass estimates from the 368 subplots and 23 hectares at the Howland Forest against UAVSAR data

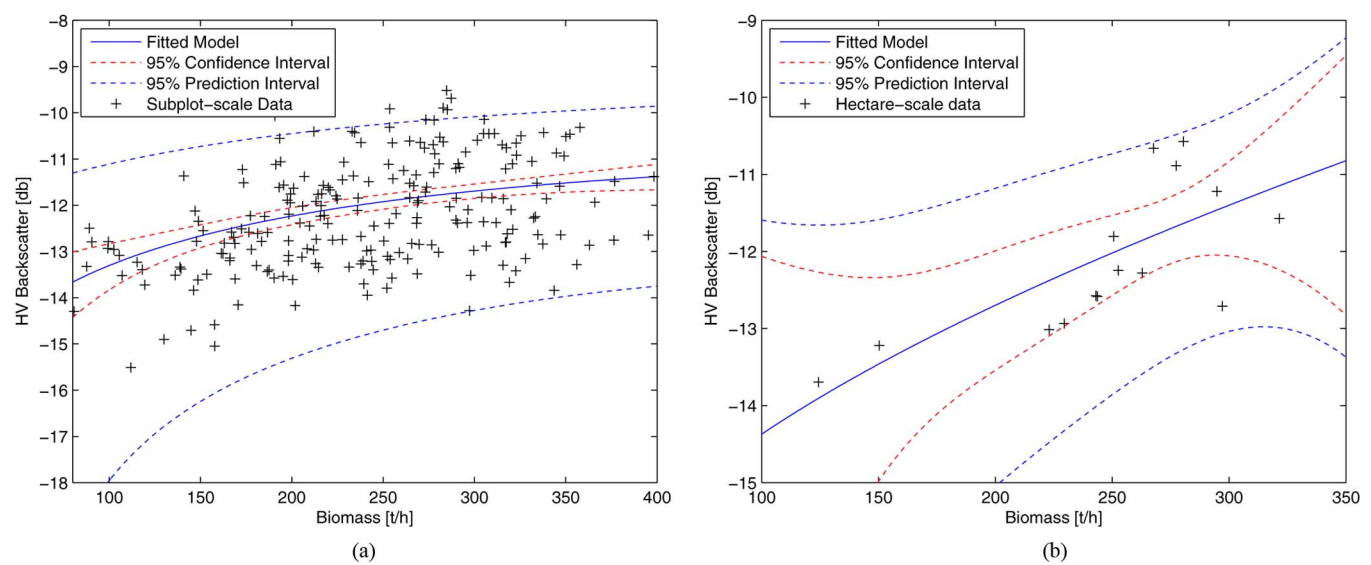


Fig. 4. Cross-polarization (HVHV) backscatter from UAVSAR plotted against field biomass estimates from the Mikaelian allometry at Harvard. (a) Subplots. (b) Hectares.

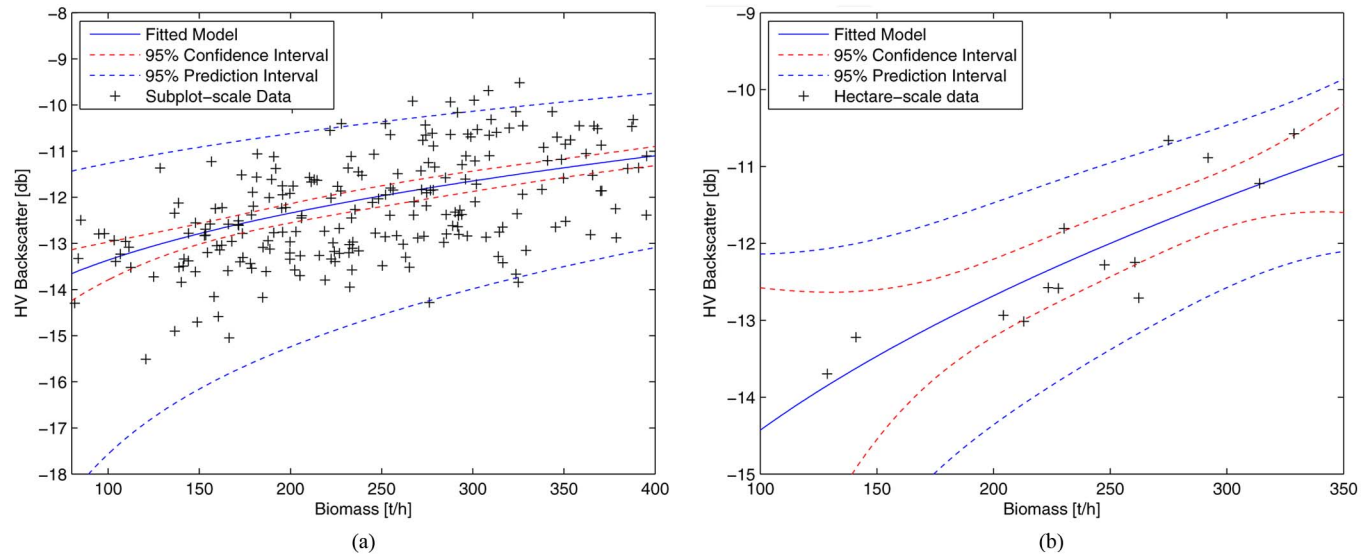


Fig. 5. Cross-pol backscatter from UAVSAR plotted against field biomass estimates from the Jenkins allometry at Harvard. (a) Subplots. (b) Hectares.

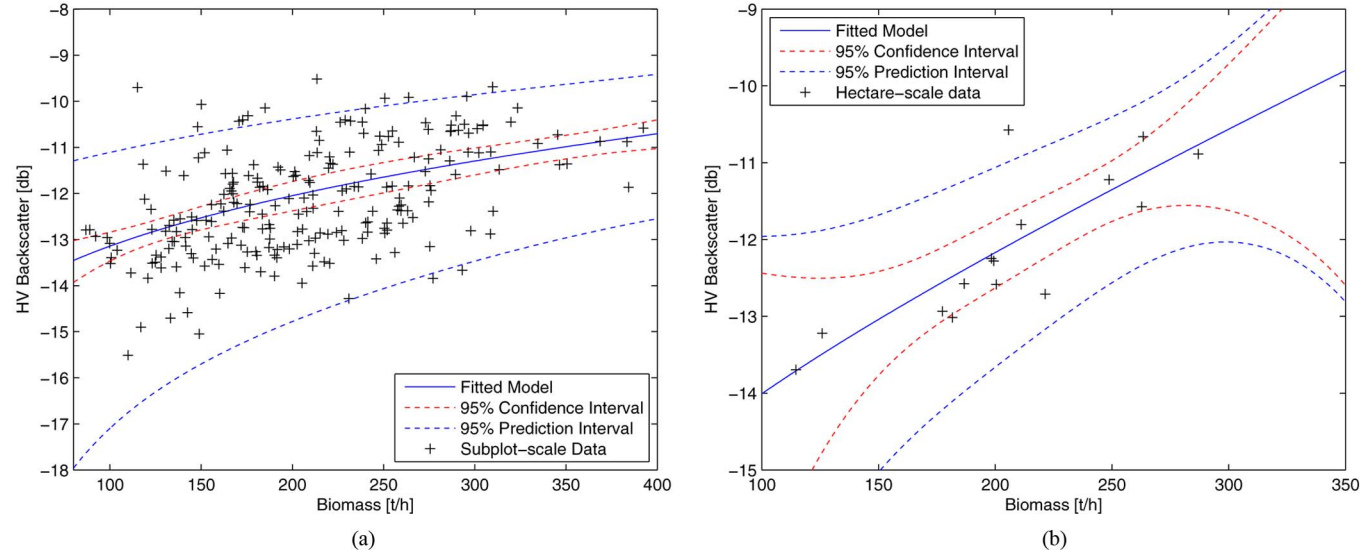


Fig. 6. Cross-pol backscatter from UAVSAR plotted against field biomass estimates from the Lambert allometry at Harvard. (a) Subplots. (b) Hectares.

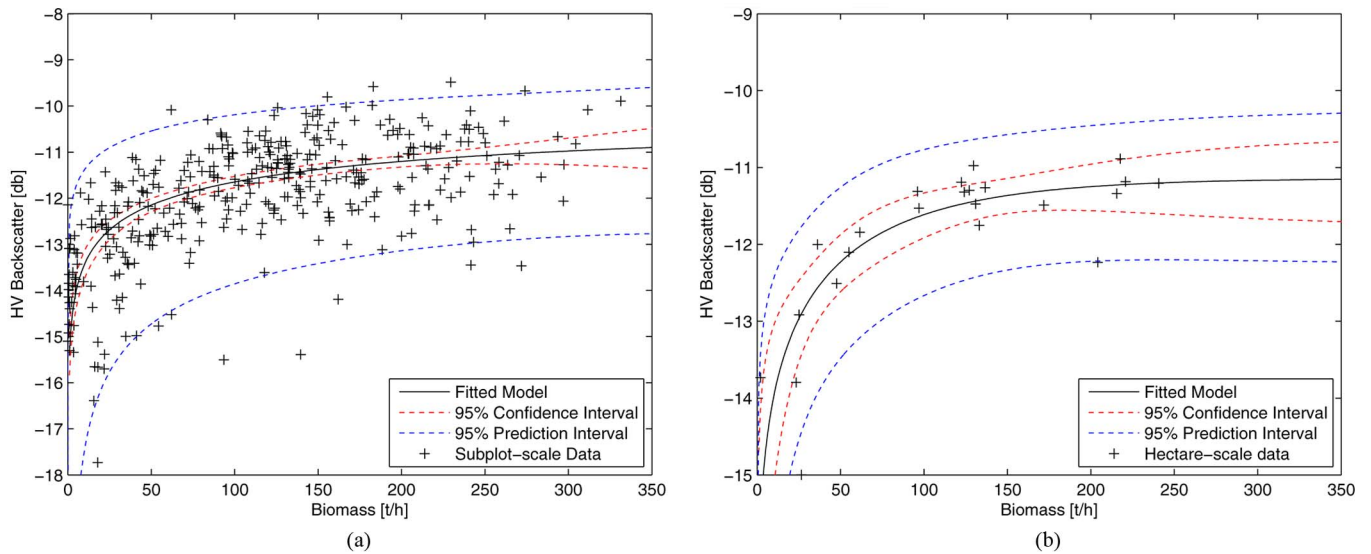


Fig. 7. Cross-pol backscatter from UAVSAR plotted against field biomass estimates from the Mikaelian allometry at Howland. (a) Subplots. (b) Hectares.

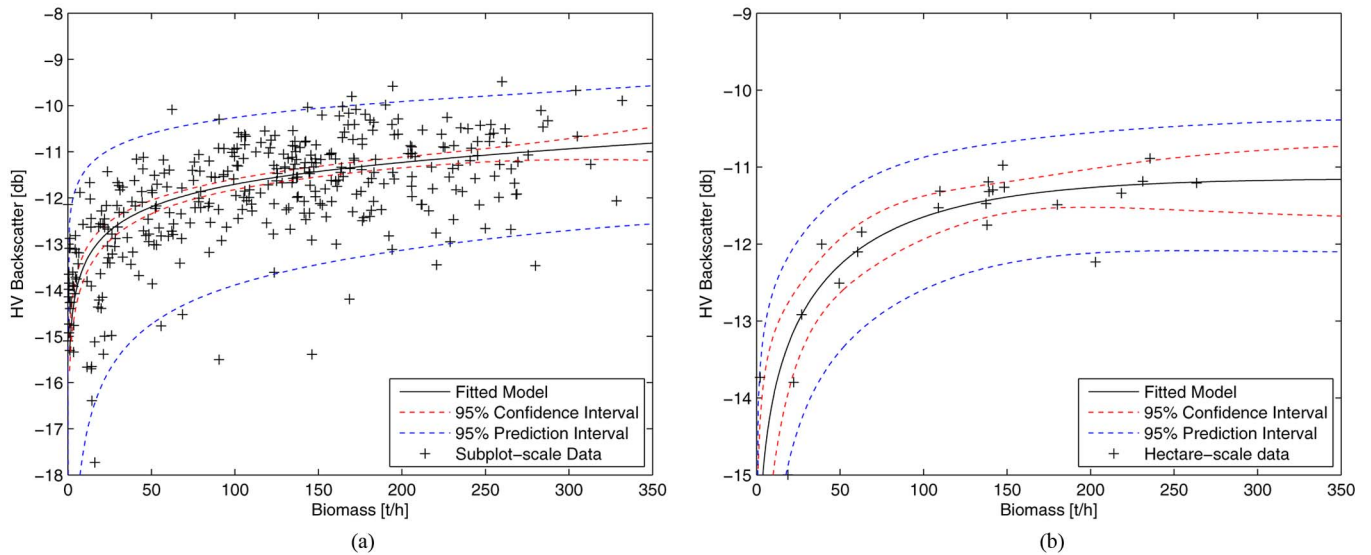


Fig. 8. Cross-pol backscatter from UAVSAR plotted against field biomass estimates from the Jenkins allometry at Howland. (a) Subplots. (b) Hectares.

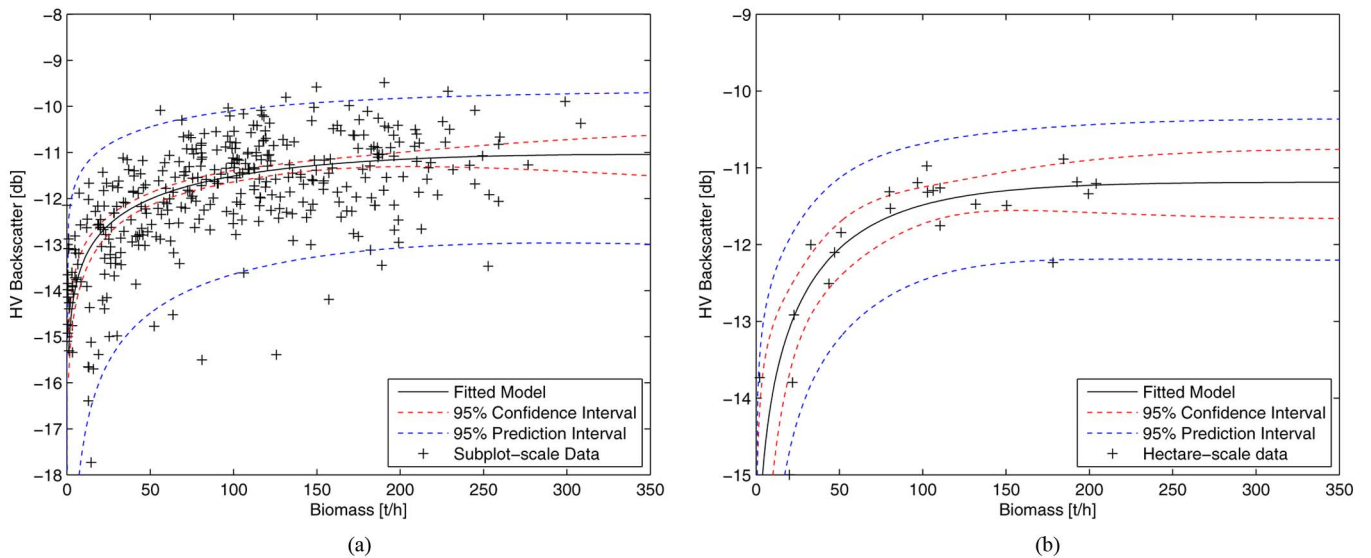


Fig. 9. Cross-pol backscatter from UAVSAR plotted against field biomass estimates from the Lambert allometry at Howland. (a) Subplots. (b) Hectares.

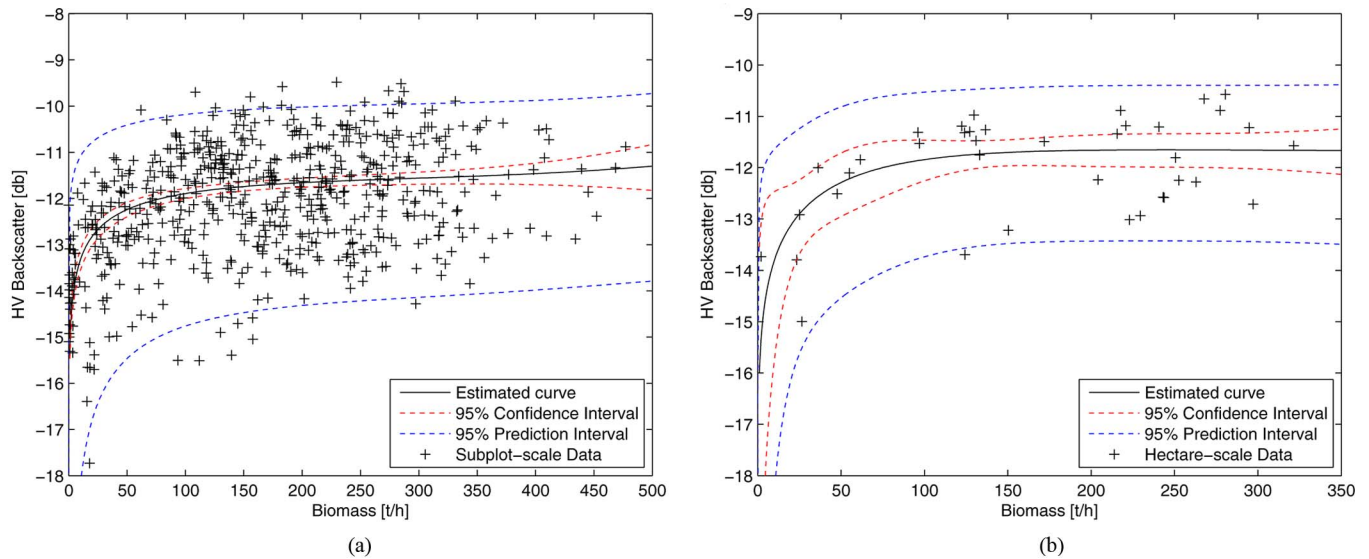


Fig. 10. Backscatter from UAVSAR plotted against field biomass estimates from the Mikaelian allometry for data combined from the two sites. (a) Subplots. (b) Hectares.

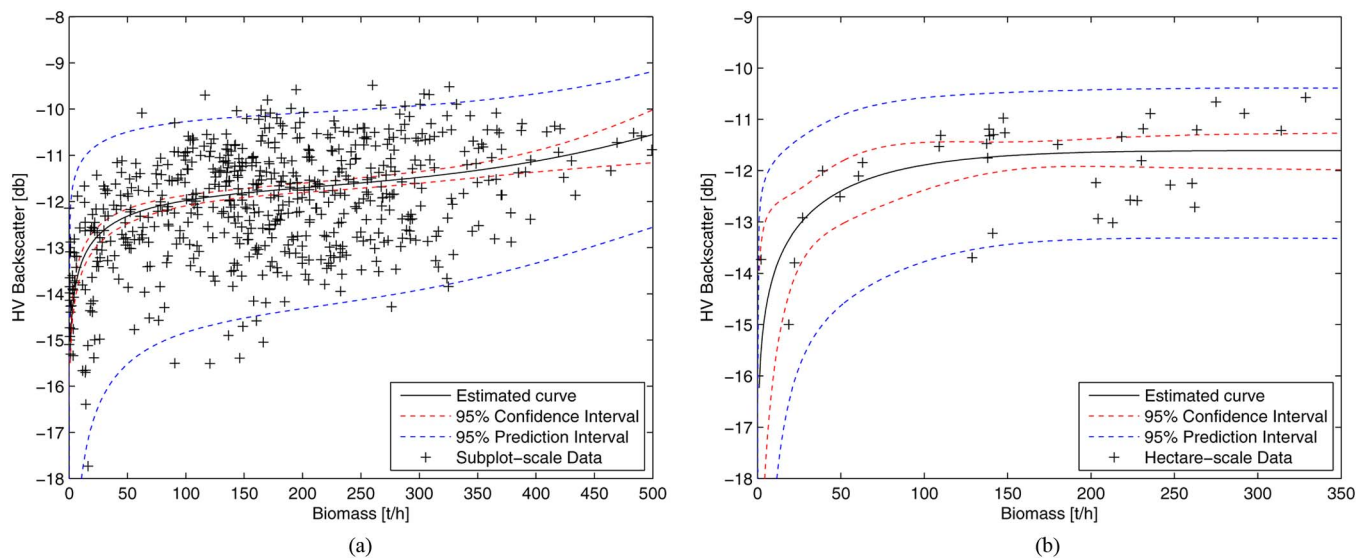


Fig. 11. Backscatter from UAVSAR plotted against field biomass estimates from the Jenkins allometry for data combined from the two sites. (a) Subplots. (b) Hectares.

from ten scenes processed from lines listed in Table II. Because of the similarity in radar observations and field campaigns, the number of looks, N , and number of repeat observations, N_{ot} , remain unchanged. Similar to the Harvard Forest, only cross-polarized (HVHV) data from UAVSAR are chosen for analysis here. Because of the presence of low-biomass sites in the Howland Forest data set, the fitted curve is more similar to results from published studies [33], [15]. The results at the Harvard Forest were unconventional because of the absence of any field sites with biomass values less than 80 tons/ha. The confidence and prediction intervals, however, are not that different in either cases, with the width of the interval mostly dependent on the number of observations around the particular biomass value.

C. Combining Harvard and Howland Forest Data Sets

The combined biomass values at the Harvard and Howland Forests span a much wider range, from 0 to 500 tons/ha for subplots and from 0 to 350 tons/ha for hectares. Because of the similarity of radar observations and field data, it is possible to simply combine the two data sets so that the intervals can be computed over larger ranges of biomass values. Figs. 10–12 plot the mean UAVSAR backscatter against field biomass estimates from the three allometric equations over both the Harvard and Howland Forest data sets. The backscatter–biomass curves from the three allometries over either sites individually or combined, all have the familiar saturation trend in L-band radar backscatter for biomass values higher than approximately 100 tons/ha. The confidence intervals are wider

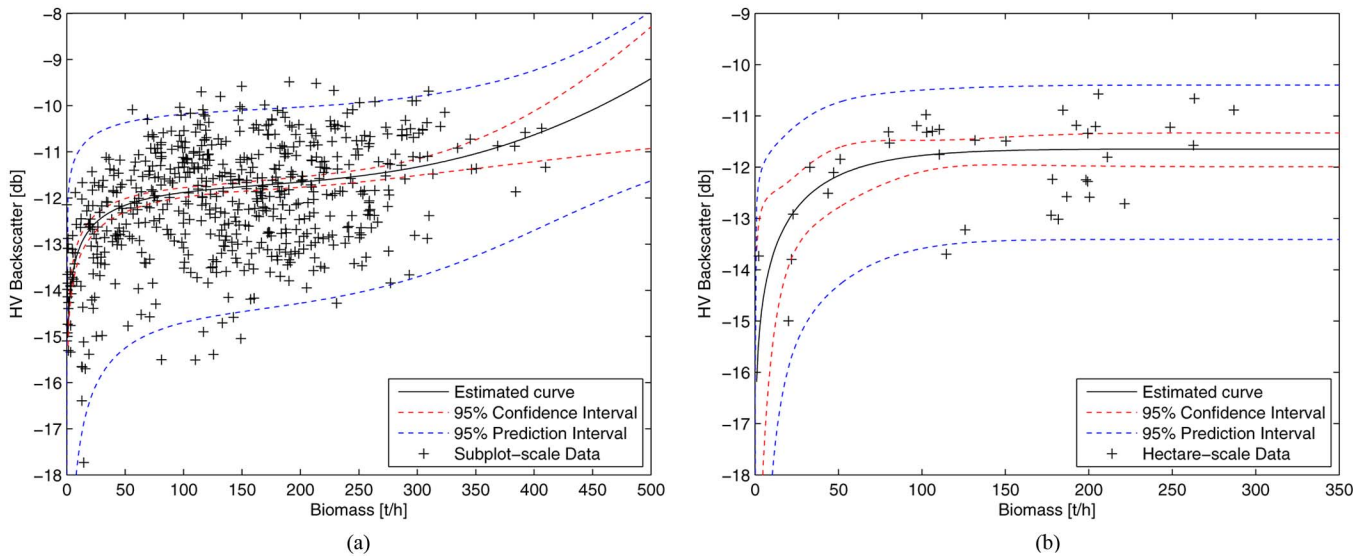


Fig. 12. Backscatter from UAVSAR plotted against field biomass estimates from the Lambert allometry for data combined from the two sites. (a) Subplots. (b) Hectares.

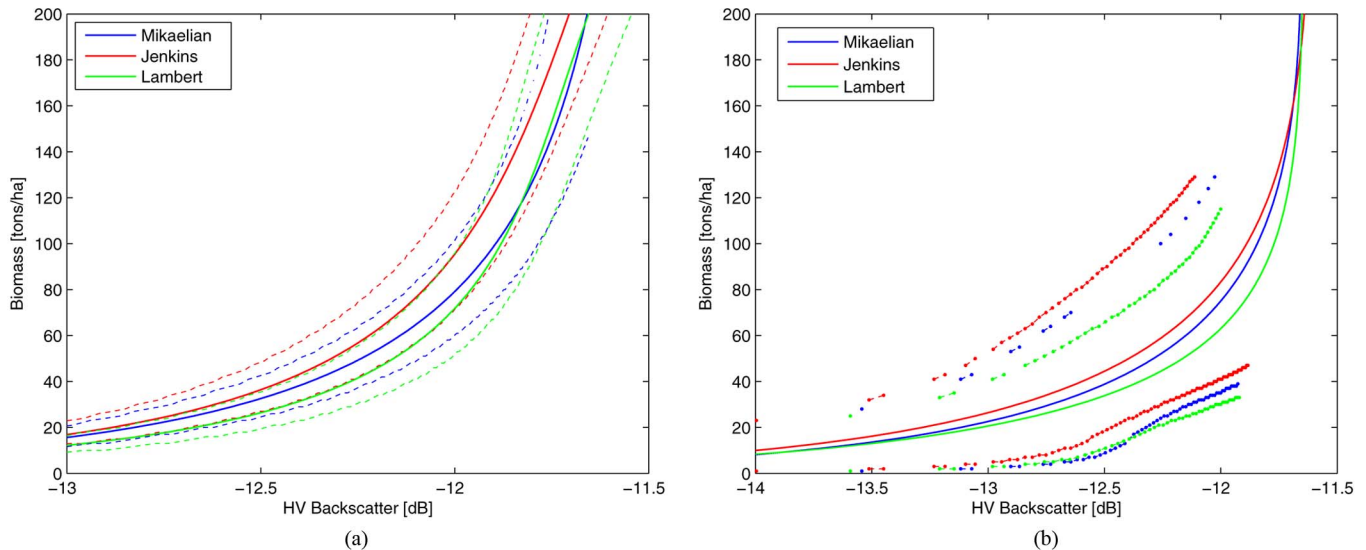


Fig. 13. Confidence intervals on biomass estimates using data from both Harvard and Howland Forests. (a) Subplots. (b) Hectares.

at hectare scales than at subplots primarily due to the larger number of samples used for regression. The prediction intervals are dominated mostly by the model error (or error in equation), which is not perfectly known but rather estimated from fit residuals. The fits for subplot-scale combined data using the Jenkins and Lambert allometries show a deviation from the saturation trend at high biomass values, where backscatter apparently increases with the increase in biomass. This, however, is an artifact of the lack of samples at such large biomass values, indicated by the substantial increase in the width of the confidence intervals. The width of these intervals would seem to suggest that subplot-level estimates are more accurate. Fig. 13 plots the inverted confidence intervals for the three allometries for the combined data set. As such, the confidence intervals on subplot-level estimates are much tighter, and because of the nonsaturated nature of the fits, the intervals do exist for larger biomass values. At hectare scales, however, the confidence intervals are much wider. Furthermore, due

to the saturated nature of the curves at these spatial scales, the intervals are infinitely large at biomass values larger than 80 tons/ha. The width of prediction intervals for either of the sites or allometries is large enough that a numerical inversion leads to infinitely large biomass-prediction intervals over all biomass values.

A first glance at the results displayed in Fig. 13 would suggest that subplot-scale biomass estimates from radar backscatter are more accurate; however, such a conclusion seems counterintuitive. Averaging should reduce error in biomass estimates, which does not seem to be the case. The width of the confidence intervals seems only to be guided by the number of samples. The reason for this discrepancy is the exclusion of measurement error from this discussion. The covariance matrix $\hat{\Sigma}_\beta$ assumes no difference between the errors in subplot or hectare-scale measurements of either biomass or backscatter. Any realistic confidence or prediction interval must therefore include a treatment of measurement error.

TABLE III
UAVSAR HARDWARE AND PROCESSING-SPECIFIC VARIABLES NEEDED
FOR COMPUTING ERROR IN BACKSCATTER MEASUREMENTS

Parameter	Value	Description [units]
B	80	Radar Bandwidth [MHz]
σ_0	-40	Noise equivalent sigma nought [dB]
b	8	Quantization level [bits]
η_ρ	0.7	Range impulse weighting factor
η_s	0.7	Azimuth impulse weighting factor
L_{az}	1.5	Antenna azimuth length [m]
k	1/88	beam shaping factor
$\theta_{1/2,s}$	8	Azimuth 3-dB beamwidth [degrees]
$\theta_{1/2,e}$	39	Elevation 3-dB beamwidth [degrees]
AMB_t	20	Total Ambiguities [dB] [21]
$\Delta\sigma_{dB}$	0.05	Random calibration errors [dB] [21]
$\Delta\theta$	0.8	Pointing uncertainty [dB]
Δh_{dem}	3	DEM accuracy [m]
L_{dem}	30	DEM posting [m]
$\Delta\rho$	1.875	Range resolution [m], Equation (23)
Δs	0.75	Azimuthal resolution [m], Equation (24)
$\kappa_{\rho,s}$	1.1909	Beam broadening factor, Equation (25)
A_{pix}	1.4062	SLC pixel area ($\Delta s \times \Delta\rho$) [m ²]
A_{dem}	900	DEM pixel area (L_{dem}^2) [m ²]

TABLE IV
OBSERVATION-SPECIFIC VARIABLES NEEDED FOR COMPUTING
ERROR IN BACKSCATTER MEASUREMENTS

Parameter	Value	Description [units]
N_{oi}	10	number of speckle identical observations
N_{os}	1	number of speckle diverse observations
A_g	10000	Area of field site (hectares) [m ²]
θ_i	40	local incidence angle (mean) [degrees]
τ_ρ	3	Mean cross track slope [degrees]
τ_s	3	mean azimuth slope [degrees]
N	3223	number of spatial looks, Equation (22)
ρ	16322	range to target [m]
$\Delta\theta_{dem}$	0.183	Pointing error from DEM [mm], Equation (35)
$\Delta\tau_x$	0.0997	Error in range, azimuth slopes [m], Equation (38)

D. Accounting for Measurement Error

With the detailed discussion of error in measuring field biomass presented earlier, this section is devoted to the estimation of the error in radar backscatter using the theoretical framework presented in Section II-D and [21]. Other than temporal variability, the components of backscatter error can be calculated from information about the instrument and knowledge of observation geometry. For UAVSAR data, most of these variables can be obtained from annotation files distributed with the data and are listed in Tables III and IV. Table III lists the parameters with which UAVSAR data were acquired and processed over the Harvard and Howland Forest sites during the two field campaigns, while Table IV lists the parameters specific to the field sites and the scenes chosen for this analysis. Since the DEM distributed along with UAVSAR data is derived from SRTM, the DEM-related parameters such as posting and accuracy are from [34]. The two parameters in Table III not readily available from the annotation files, AMB_t (total ambiguity ratio) and $\Delta\sigma_{dB}$ (random calibration errors), are based on values in [21].

1) *Analyzing Temporal Variability:* A definitive model that describes temporal variation in radar backscatter does not yet exist, mainly due to its complex nature. However, it could be a significant error source, so it must be characterized. It is

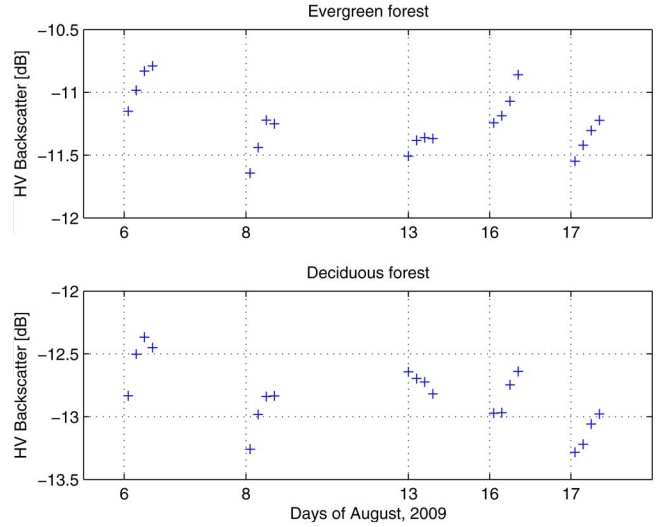


Fig. 14. Cross-polarized backscatter UAVSAR data from 20 ascending lines over two regions of mostly evergreens and deciduous trees near the Harvard Forest.

possible to do so for a specific data set, such as that over the Harvard and Howland Forests, where data collection happened over short enough time scales so that factors such as seasonal and anthropogenic change can be ignored. Physical factors that are expected to still impact backscatter include weather events such as rain or wind, moisture variations in the soil, or the canopy during the day. Over the Harvard Forest, UAVSAR acquired data over five days in August of 2009, the 6th, 8th, 13th, 16th, and 17th. Fig. 14 plots average cross-polarized backscatter data over two regions of evergreens and deciduous trees (roughly three hectares each) near the Harvard Forest from 20 ascending lines (5° heading). The two regions, chosen from optical imagery in *leaf-off* conditions, consist of roughly 8000 UAVSAR looks, enough to significantly reduce speckle while allowing the regions to remain homogeneous. While there is an overall lack of trend in backscatter over the eleven-day period, however, within a single day, the backscatter values seem to increase with time for both types of forests and all of the acquisition dates except the 13th. Incidence angle variation could be the reason since these lines were acquired with varying baselines for repeat-pass interferometric observations. However, not only are the incidence angle variations insignificant enough to cause this trend, the lines were designed such that the incidence angle would increase with each line (hence time) which should theoretically cause a decrease in backscatter intensity [29]. The absence of trend on the 13th could be attributed to the fact that there was significant precipitation for most of that day with rain as high as 13 dBz at the time of acquisition. The change in moisture of either the soil, trunk, or the canopy seems to be the most likely reason for the backscatter trend observed over the other days.

Since the look geometry does not vary significantly for these scenes, the contribution to the variation seen in Fig. 14 from pointing errors is negligible. Furthermore, with a large number of looks, the contribution of speckle and thermal noise is also minimal. In the absence of a well-defined model of temporal variation, once the errors due to DEM uncertainties have been removed, the sample variance seen over these 20 lines serves

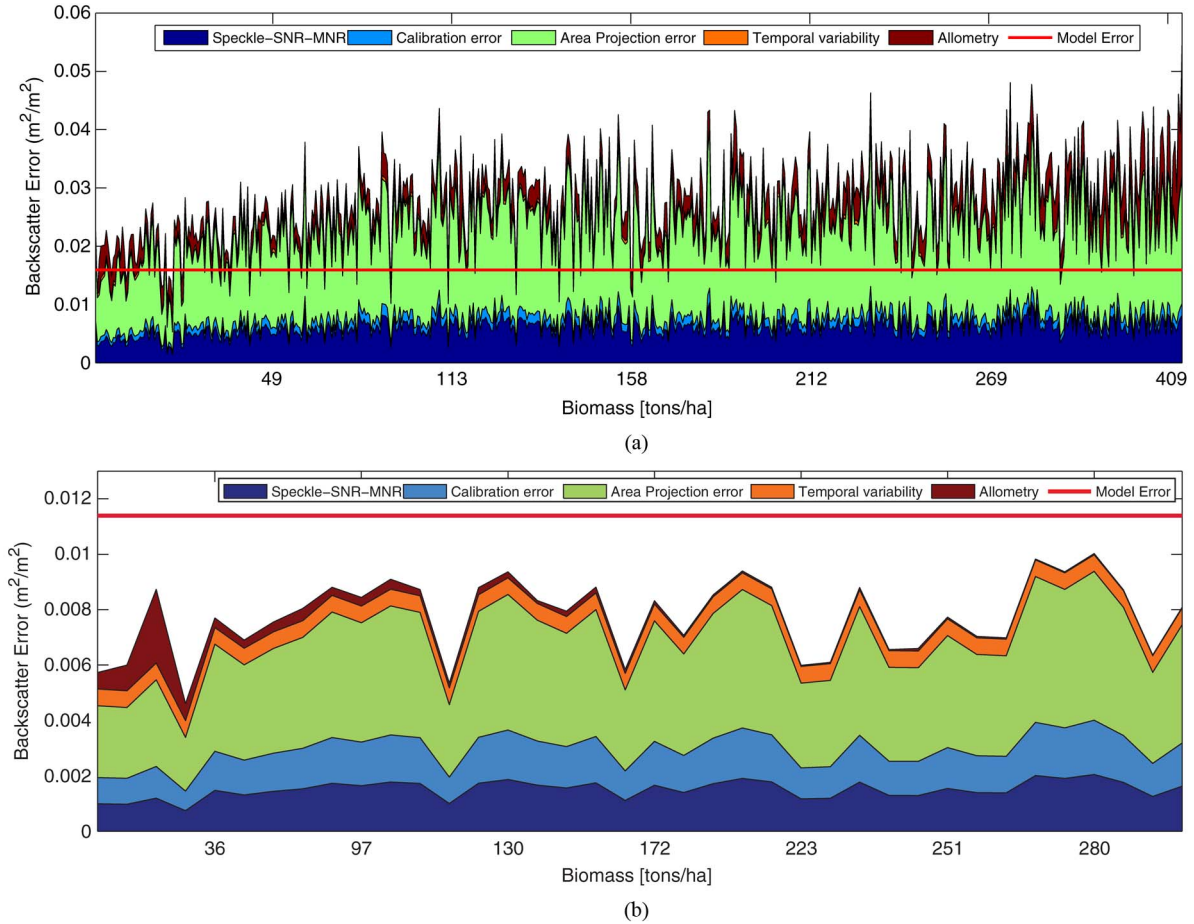


Fig. 15. Subplot and hectare-scale errors in backscatter for the combined data set over Harvard and Howland Forests. Also plotted are model errors and allometric errors (in field biomass using the Mikaelian [8] equations) projected into units of radar backscatter using fitted coefficients. (a) Subplots. (b) Hectares.

as an estimate of error induced from temporal variations in cross-polarized UAVSAR backscatter data from this particular campaign. Here, this error term is approximated by assuming that the rms variation seen in the data over the eleven-day period captures the temporal variation, which is on the order

$$\Delta\sigma_t = 0.002 \text{ m}^2/\text{m}^2. \quad (44)$$

With this approximation, the error in radar backscatter measurements can be computed for the particular viewing geometry and field sites over the Harvard and Howland Forests. Fig. 15 plots the estimated total error in backscatter and its components, *speckle-SNR-MNR* ($\Delta\sigma_s$), *calibration error* ($\Delta\sigma_c$), *area projection error* ($\Delta\sigma_a$), and *temporal variability* ($\Delta\sigma_t$), for the field sites at both the hectare and subplot scales. Also plotted are the allometric errors, converted to backscatter units using

$$\Delta\sigma_{mi} = \left. \frac{\partial\sigma}{\partial M} \right|_{M_i} \Delta M_i \quad i = 1, \dots, n \quad (45)$$

where σ is the backscatter modeled as a function of biomass given in (1) and M is the field biomass. The number of measurements, n , vary with spatial scales. At hectares, $n = 38$ for a total of 38 hectares from the combined data set over the Harvard and Howland Forests, while $n = 608$ for subplot scales (with 16 subplots per hectare). For comparison, Fig. 15

also plots the model error, estimated from the rms value of the residuals from the naive fits (where measurement error is not considered). The absolute error in radar backscatter at subplot scales is almost an order of magnitude higher, primarily due to the decrease in the number of looks by a factor of 16. However, note that the backscatter measurement error at subplot scales is almost always larger than the estimated model error, while the model error dominates at hectare scales. Furthermore, the backscatter measurement error at subplot scales is comparable to the dynamic range of the backscatter values over the field sites. The largest contribution to the radar error budget in either cases is from uncertainties in area projection that arise from the use of the 30-m SRTM DEM to correct a meter-scale UAVSAR pixel. This error would reduce significantly if a better resolved or more accurate DEM were to be used.

As discussed in Section II-C, there are two aspects to obtaining measurement-error-corrected confidence bounds: estimating bias in regression coefficients and bootstrapping estimates of confidence intervals using the unbiased coefficients. Fig. 16 shows the results of the SIMEX analysis conducted on the coefficients of the backscatter-biomass model in (1) using the modeled measurement errors in radar backscatter and field biomass for hectare-scale plots. The SIMEX method estimates unbiased coefficients by evaluating the quadratic fits to $\hat{\beta}_i(\lambda)$ at $\lambda = -1$. Fig. 16 shows the trend in each of the regression variables as a function of λ and their respective quadratic fits

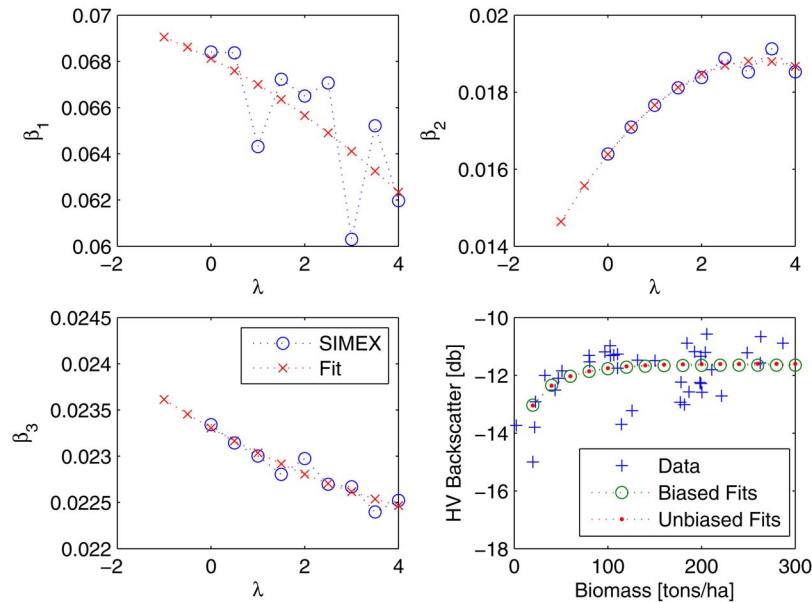


Fig. 16. Estimation of bias introduced by measurement error on the fit coefficients using SIMEX. Fits using biased and unbiased coefficients are plotted as well.

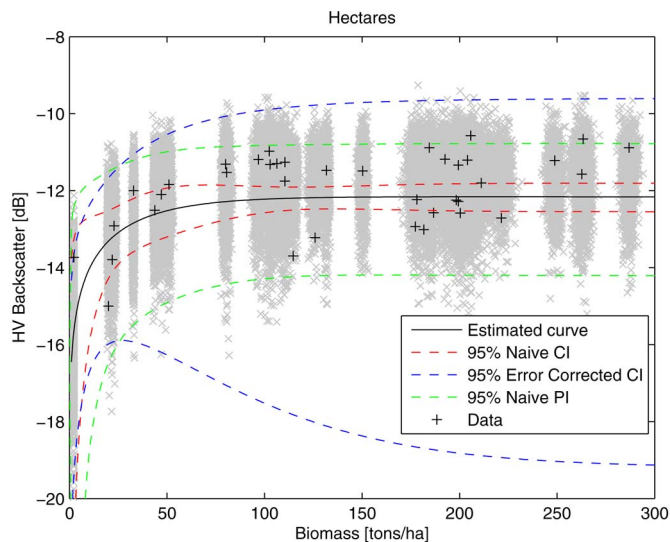


Fig. 17. Cross-pol backscatter from UAVSAR plotted against field biomass estimates from the Lambert allometry [10] for data combined from the two sites. Confidence intervals from the naive fits as well as the ones corrected for modeled measurement error are shown.

that are extended to $\lambda = -1$. Predicted backscatter values from both the biased and the unbiased set of coefficients, shown in the bottom-right panel of Fig. 16, indicate that measurement error does not introduce a significant bias to the predicted backscatter. At subplot scales, with measurement errors in radar backscatter that are comparable to the dynamic range of cross-polarized data over the two field sites, the SIMEX starts to falter because of the failure of iterative fitting algorithms to converge frequently. With enough such failures, SIMEX results become untrustworthy, which is the case with subplot-scale data over the Harvard and Howland Forests. Fig. 17 shows the measurement-error-corrected confidence intervals estimated using the parametric bootstrap method for hectare-scale data over the two sites. The gray cloud of points is the sim-

ulated data sets (for $B = 1000$). The width of the confidence interval estimated from the bootstrap method is much larger than the width of the naive confidence interval (where measurement error is not considered). In fact, the confidence interval is wider than the naive prediction interval as well, indicating that the impact of measurement error is fairly significant. The confidence intervals from the two other allometries are similarly wide. These bounds are large enough such that they cannot be inverted to obtain confidence intervals on biomass estimates from the radar. This would suggest that, if the bootstrapped intervals are to be trusted, the combination of large model error and measurement error in radar backscatter reduces the confidence in biomass estimates from radar backscatter to the point that such estimates over the Northeastern United States would be of very low quality.

E. Analyzing Model Error

Fig. 15 shows that, at hectare scales, the model error is larger than the total measurement error and is consequently the dominant contributor to the width of the measurement-error-corrected confidence intervals. Unlike the species-specific regression equations used in [16], the backscatter–biomass model in (1) makes no such distinction. The UAVSAR backscatter data over the Harvard and Howland Forests, however, are distinctly different between areas dominated by deciduous trees and areas of mostly coniferous trees. Areas of deciduous trees appear darker than the coniferous trees in the cross-polarized UAVSAR imagery, most likely due to the amount of attenuation caused by the larger moisture content in the deciduous tree canopies, by as much as 1 dB.

Fig. 18 shows the difference in backscatter between the two forest types for the hectare-scale field sites. The hectare plots are classified as softwoods or hardwoods based on the biomass contribution of each type of tree to the total biomass of the hectare, with a majority defined as 60% or more. Field

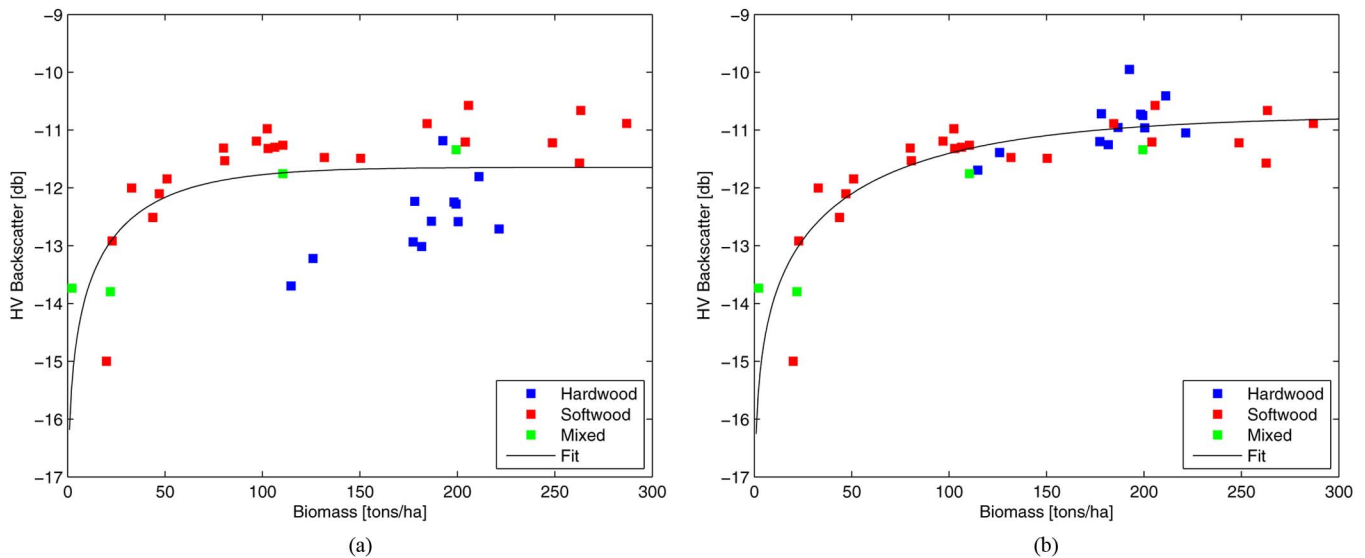


Fig. 18. Impact of species on the relationship between backscatter and field biomass over the Harvard and Howland Forests. (a) Unaltered. (b) With offset.

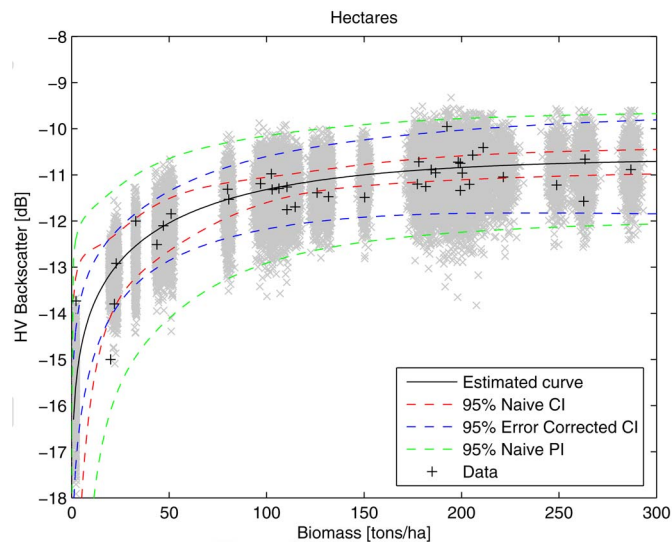


Fig. 19. Measurement-error-corrected confidence intervals using the Lambert [10] allometry.

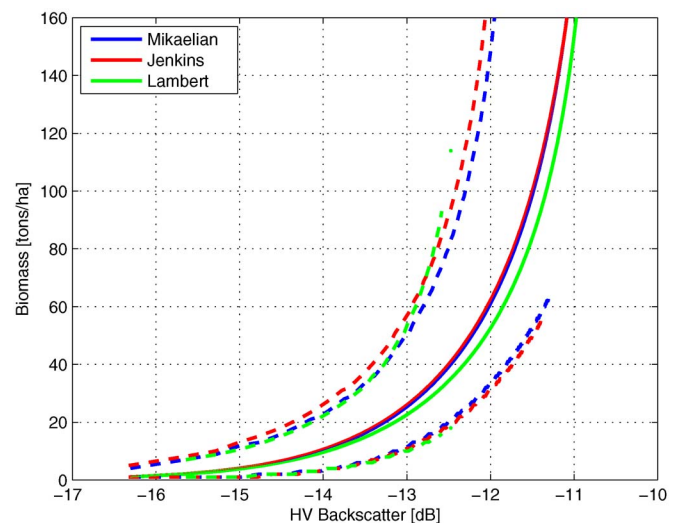


Fig. 20. Measurement-error-corrected confidence intervals on biomass estimates from radar backscatter for the three allometric equations Mikaelian [8], Jenkins [9], and Lambert [10].

sites where the biomass contribution of either forest types is not more than 60% of the total biomass are classified as mixed forest. The grouping of hardwoods and softwoods is quite apparent in Fig. 18(a), with the hardwood-dominated sites lower in backscatter value than the softwood sites with similar biomass by a decibel or so. Fig. 18(b) plots UAVSAR data where the backscatter from hardwoods has been offset by a backscatter coefficient value of $0.025 \text{ m}^2/\text{m}^2$. This particular bias value has been chosen by looking at the average offset between regions of hardwoods and softwoods. This offset is not guided by scattering models, but rather, it was chosen to minimize the impact of species dependence of backscatter on model error. In reality, the physical backscatter–biomass models ought to be species dependent [16] and capable of accounting for seasons. Such models would likely account for this offset in a more elegant manner; however, having multiple models complicates the statistical framework significantly, so

for a cursory analysis of residuals, this approach suffices. By adding this offset, the rms residuals reduce significantly, from a value of 0.0113 to $0.007 \text{ m}^2/\text{m}^2$, a factor of two reductions. Fig. 19 plots the measurement-error-corrected intervals at hectare scales using the Lambert [10] allometry with the backscatter intensity values of hardwood-dominated hectares offset by $0.025 \text{ m}^2/\text{m}^2$. The error-corrected intervals shown here are much narrower compared to those seen in Fig. 17, highlighting the impact of model error on the confidence intervals. Fig. 20 plots the backscatter–biomass model and numerically inverted confidence bounds for the three allometric equations using the corrected data. The asymmetric confidence intervals are not invertible after 60 tons/ha, primarily due to the saturation in radar backscatter at higher biomass values. However, even where these confidence intervals are invertible, they are quite wide, suggesting that, even though backscatter can predict low biomass, the quality of these estimates would still be low.

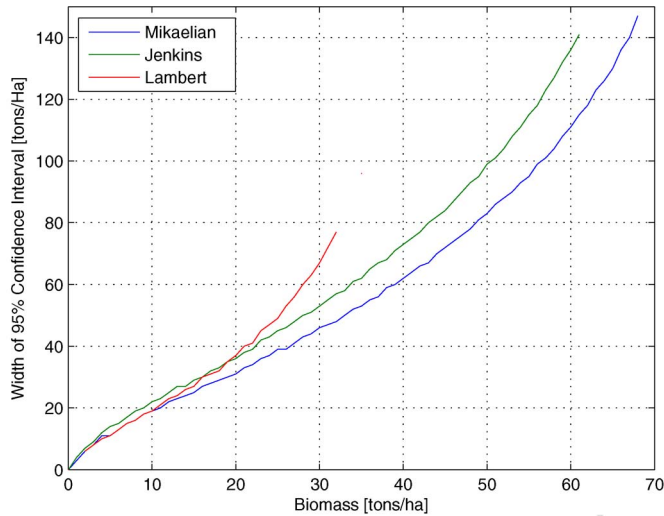


Fig. 21. Width of the confidence intervals on biomass estimates obtained from radar backscatter using the three allometric equations Mikaelian [8], Jenkins [9], and Lambert [10].

Fig. 21 shows the width of the 95% confidence interval on biomass estimates as a function of the radar-derived mean biomass. The width of the confidence interval is always larger than the mean value of the biomass estimate itself, highlighting further the low quality of radar-derived backscatter estimates over the Harvard and Howland Forests even at low-biomass levels where radar backscatter is expected to perform best.

IV. CONCLUSION

In this paper, a rigorous statistical framework for estimating the quality of biomass estimates obtained from radar backscatter incorporating measurement errors in both field biomass and radar backscatter was established. Techniques for calculating confidence intervals in a nonlinear-regression scenario with measurement error, such as the case when estimating biomass from radar backscatter, were discussed. A model for estimating the error in radar measurements was outlined. The calculation of the errors in radar measurements from the UAVSAR field campaigns over the Harvard and Howland Forests based on the error model and instrument information was discussed. Results of the regression analysis between field estimates of biomass and backscatter data from the UAVSAR field campaign over the Harvard and Howland Forests show that measurement-error-corrected confidence intervals from the nonlinear backscatter–biomass model are wide enough that they cannot be inverted to obtain the corresponding intervals on biomass estimates from radar backscatter at either the hectare or subplot scales. The reasons for the large confidence interval widths are twofold: a) the saturation of the backscatter–biomass curve and b) combination of large model error and measurement error in radar backscatter. An analysis of the model error shows that a distinct bias in backscatter value between the deciduous and coniferous trees contributes to an increase in model error variance. Removing the bias in backscatter between the two forest types reduces model error and consequently

allows for the estimation of confidence bounds on biomass estimates. However, the confidence intervals can only be estimated at hectare scales; at subplot scales, the measurement error in radar backscatter tends to dominate and cause the bootstrap method to fail. The width of confidence bounds at hectare scales over the Harvard and Howland Forests shows that the errors in biomass estimates from cross-polarized radar backscatter (which was found to be most sensitive to biomass) from the L-band UAVSAR data are around 100% even at low-biomass levels. While this study focuses primarily on the forests of New England, the results likely will have broader implications on the quality of global carbon mapping using radar backscatter. However, similar rigorous studies that focus on different biomes and observation scenarios are needed to better characterize the performance of radar backscatter as a means of mapping forest biomass.

REFERENCES

- [1] R. Anthes, *Earth Science and Applications from Space: National Imperatives for the Next Decade and Beyond*, National Research Council Committee on Earth Science and Applications from Space. Washington, DC, USA: National Academic Press, 2007.
- [2] F. G. Hall, K. Bergen, J. B. Blair, R. Dubayah, R. Houghton, G. Hurtt, J. Kellndorfer, M. Lefsky, J. Ranson, S. Saatchi, H. Shugart, and D. Wickland, "Characterizing 3D vegetation structure from space: Mission requirements," *Remote Sens. Environ.*, vol. 115, no. 11, pp. 2753–2775, Nov. 2011.
- [3] R. Ahmed, P. Siqueira, S. Hensley, and K. Bergen, "Uncertainty of forest biomass estimates in north temperate forests due to allometry: Implications for remote sensing," *Remote Sens.*, vol. 5, no. 6, pp. 3007–3036, Jun. 2013.
- [4] R. T. Fisher, "The management of the Harvard Forest," in *Harvard Forest Bulletin*. Petersham, MA, USA: Harvard Forest, 1921, pp. 1–55.
- [5] R. H. Whittaker, F. H. Bormann, G. E. Likens, and T. G. Siccama, "The Hubbard Brook ecosystem study: Forest biomass and production," *Ecol. Monogr.*, vol. 44, no. 2, pp. 233–254, Spring 1974.
- [6] H. E. Young, J. H. Ribe, and K. Wainwright, "Weight tables for tree and shrub species in Maine," in *Life Sciences and Agriculture Experiment Station*. Orono, ME, USA: Univ. of Maine, 1980, Miscellaneous Report.
- [7] B. Stout, "Species distribution and soils in the Harvard Forest," in *Harvard Forest Bulletin*. Petersham, MA, USA: Harvard Forest, 1952, pp. 1–29.
- [8] M. T. Ter-Mikaelian and M. D. Korzukin, "Biomass equations for sixty-five North American tree species," *Forest Ecol. Manage.*, vol. 97, no. 1, pp. 1–24, Sep. 1997.
- [9] J. Jenkins, D. Chojnacky, L. Heath, and R. Birdsey, "National-scale biomass estimators for United States tree species," *Forest Sci.*, vol. 49, no. 1, pp. 12–35, Feb. 2003.
- [10] M. Lambert, C. H. Ung, and F. Raulier, "Canadian national tree above-ground biomass equations," *Can. J. Forest Res.*, vol. 35, no. 8, pp. 1996–2018, Aug. 2005.
- [11] I. S. Alemdag and J. Richardson, "Annotated bibliography of ENFOR biomass reports 1979–1990," Forestry Canada, Ottawa, ON, Canada, ser. Inf. Rep. ST-X-6, 1993.
- [12] E. P. W. Attema and F. T. Ulaby, "Vegetation modeled as a water cloud," *Radio Sci.*, vol. 13, no. 2, pp. 357–364, Mar./Apr. 1978.
- [13] J. A. Richards, G. Q. Sun, and D. S. Simonet, "L-band radar backscatter modeling of forest stands," *IEEE Trans. Geosci. Remote Sens.*, vol. GE-25, no. 4, pp. 487–498, Jul. 1987.
- [14] S. T. Wu, "Potential application of multi-polarization SAR for plantation pine biomass estimation," *IEEE Trans. Geosci. Remote Sens.*, vol. GE-25, no. 3, pp. 403–409, May 1987.
- [15] T. Le Toan, A. Beaudoin, J. Riom, and D. Guyon, "Relating forest biomass to SAR data," *IEEE Trans. Geosci. Remote Sens.*, vol. 30, no. 2, pp. 403–411, Mar. 1992.
- [16] M. C. Dobson, F. T. Ulaby, L. E. P. adn, T. L. Sharik, K. M. Bergen, J. Kellndorfer, J. R. Kendra, E. Li, Y. C. Lin, A. Nashashibi, K. Sarabandi, and P. Siqueira, "Estimation of forest biophysical characteristics in northern Michigan with SIR-C/X-SAR," *IEEE Trans. Geosci. Remote Sens.*, vol. 33, no. 4, pp. 877–895, Jul. 1995.

- [17] A. Luckman, J. Baker, T. M. Kuplich, C. da Costa Freitas Yanasse, and A. C. Frery, "A study of the relationship between radar backscatter and regenerating tropical forest biomass for spaceborne SAR instruments," *Remote Sens. Environ.*, vol. 60, no. 1, pp. 1–13, Apr. 1997.
- [18] A. Luckman, J. Baker, M. Honzk, and R. Lucas, "Tropical forest biomass density estimation using JERS-1 SAR: Seasonal variation, confidence limits, and application to image mosaics," *Remote Sens. Environ.*, vol. 63, no. 2, pp. 126–139, Feb. 1998.
- [19] R. Lucas, J. Armston, R. Fairfax, R. Fensham, A. Accad, J. Carreiras, J. Kelley, P. Bunting, D. Clewley, S. Bray, D. Metcalfe, J. Dwyer, M. Bowen, T. Eyre, M. Laidlaw, and M. Shimada, "An evaluation of the ALOS PALSAR L-band backscatter—Above ground biomass relationship Queensland, Australia: Impacts of surface moisture condition and vegetation structure," *IEEE J. Sel. Topics Appl. Earth Observ. Remote Sens.*, vol. 3, no. 4, pp. 576–593, Dec. 2010.
- [20] S. Hensley, "Desdyni biomass error model and associated spreadsheet," Jet Propulsion Laboratory (JPL), Pasadena, CA, USA, Tech. Rep., 2010, Interoffice Memorandum.
- [21] preprint S. Hensley, S. Oveisigharan, S. Saatchi, M. Simard, R. Ahmed, and Z. Haddad, A theoretical error model for biomass estimates derived from polarimetric radar 2013, preprint.
- [22] J. P. Buonaccorsi, *Measurement Error, Models, Methods and Applications*. Boca Raton, FL, USA: CRC Press, 2010.
- [23] N. R. Draper and H. Smith, *Applied Regression Analysis*, 3rd ed. Hoboken, NJ, USA: Wiley, Apr. 1998, ser. Wiley Series in Probability and Statistics.
- [24] W. A. Fuller, *Measurement Error Models*. Hoboken, NJ, USA: Wiley, 2008.
- [25] J. R. Cook and L. A. Stefanski, "Simulation-extrapolation estimation in parametric measurement error models," *J. Amer. Stat. Assoc.*, vol. 89, no. 428, pp. 1314–1328, Dec. 1994.
- [26] J. Curlander and R. McDonough, *Synthetic Aperture Radar: Systems and Signal Processing*. Hoboken, NJ, USA: Wiley, 1991, ser. Wiley Series in Remote Sensing.
- [27] S. Hensley, K. Wheeler, G. Sadowy, C. Jones, S. Shaffer, H. Zebker, T. Miller, B. Heavey, E. Chuang, R. Chao, K. Vines, K. Nishimoto, J. Prater, B. Carrico, N. Chamberlain, J. Shimada, M. Simard, B. Chapman, R. Muellerschoen, C. Le, T. Michel, G. Hamilton, D. Robison, G. Neumann, R. Meyer, P. Smith, J. Granger, P. Rosen, D. Flower, and R. Smith, "The UAVSAR instrument: Description and first results," in *Proc. IEEE RADAR Conf.*, May 2008, pp. 1–6.
- [28] A. Freeman, "SAR calibration: An overview," *IEEE Trans. Geosci. Remote Sens.*, vol. 30, no. 6, pp. 1107–1121, Nov. 1992.
- [29] F. T. Ulaby, R. K. Moore, and A. K. Fung, *Microwave Remote Sensing, Active and Passive*. Norwood, MA, USA: Artech House, 1986.
- [30] T. Castel, A. Beaudoin, N. Stach, N. Stussi, T. L. Toan, and P. Durand, "Sensitivity of space-borne SAR data to forest parameters over sloping terrain: Theory and experiment," *Int. J. Remote Sens.*, vol. 22, no. 12, pp. 2351–2376, Aug. 2001.
- [31] L. Ulander, "Radiometric slope correction of synthetic-aperture radar images," *IEEE Trans. Geosci. Remote Sens.*, vol. 34, no. 5, pp. 1115–1122, Sep. 1996.
- [32] S. Hensley, E. Chapin, and T. R. Michel, "Improved processing of AIR-SAR data based on the GeoSAR processor," presented at the Proc. AIR-SAR Earth Sci. Appl. Workshop, Pasadena, CA, USA, Mar., 2002, T3.
- [33] M. L. Imhoff, "Radar backscatter and biomass saturation: Ramifications for global biomass inventory," *IEEE Trans. Geosci. Remote Sens.*, vol. 33, no. 2, pp. 511–518, Mar. 1995.
- [34] T. G. Farr, P. A. Rosen, E. Caro, R. Crippen, R. Duren, S. Hensley, M. Kobrick, M. Paller, E. Rodriguez, L. Roth, D. Seal, S. Shaffer, J. Shimada, J. Umland, M. Werner, M. Oskin, D. Burbank, and D. Alsdorf, "The shuttle radar topography mission," *Rev. Geophys.*, vol. 45, no. 2, pp. RG2004-1–RG2004-33, Jun. 2007.



Razi Ahmed (M'08) received the B.S.E.E. degree from the National University of Sciences and Technology, Islamabad, Pakistan, in 2002 and the M.S. and Ph.D. degrees in electrical and computer engineering from the University of Massachusetts, Amherst, MA, USA, in 2012.

He is currently a National Aeronautics and Space Administration Postdoctoral Fellow at the Jet Propulsion Laboratory in Pasadena, CA, USA. His research interests include radar remote sensing, synthetic aperture radar interferometry and polarimetry,

and its application to remote sensing of vegetation characteristics.



Paul Siqueira (M'94) received the B.S. and M.S. degrees in electrical engineering from Iowa State University, Ames, IA, USA, in 1987 and 1989, respectively, and the Ph.D. degree from The University of Michigan, Ann Arbor, MI, USA, in 1996.

He is currently an Associate Professor with the Department of Electrical and Computer Engineering, University of Massachusetts, Amherst, MA, USA. Prior to joining the faculty at the University of Massachusetts in 2005, he was a Senior Engineer with the Radar Science and Engineering Section,

National Aeronautics and Space Administration Jet Propulsion Laboratory, Pasadena, CA, USA, and a Visiting Scientist with the Global Vegetation Monitoring Institute, European Commissions Joint Research Centre, Ispra, Italy. As an active member of the well-known Microwave Remote Sensing Laboratory, University of Massachusetts, his research interests are in microwave instrument development, microwave engineering, synthetic aperture radar interferometry, quantitative parameter estimation, and the application of these technical disciplines to addressing environmental issues related to the global carbon, water, and energy cycles.



Scott Hensley (SM'10) received the B.S. degree in mathematics and physics from the University of California, Irvine, CA, USA, and the Ph.D. degree in mathematics from Stony Brook University, Stony Brook, NY, USA, where he specialized in the study of differential geometry.

He has a broad range of expertise spanning over 20 years in radar remote sensing, including the design, performance evaluation, processing and application algorithms, calibration and data interpretation for geophysical applications in both Earth and planetary

sciences, and in managing the development of complex radar interferometric systems from inception to operational platforms including developing novel algorithms for the processing and exploitation of such systems. He has worked on most of the synthetic aperture radar systems developed at JPL over the past two decades, including the Magellan and Cassini radars. He was the Project Scientist for GeoSAR, a simultaneous X-band and P-band airborne radar interferometer for mapping above and beneath the canopy that is now commercially operated by Earthdata International. He led the SRTM Interferometric Processor Development Team for a shuttle-based interferometric radar used to map the Earth's topography between 60 latitude. Recently, he began working with the Earth-based Goldstone Solar System Radar to generate topographic maps of the lunar surface. He was the Principal Investigator and is currently the Project Scientist for the National Aeronautics and Space Administration Uninhabited Aerial Vehicle Synthetic Aperture Radar program.